

**CHARACTERIZATION AND DEVELOPMENT OF LATERAL FLOW
ASSAYS FOR AUTOMATED MULTI-STEP PROCESSES AND
POINT-OF-CARE CERVICAL CANCER DETECTION**

by

Emilie I. Newsham

A Thesis

Submitted to the Faculty of Purdue University

In Partial Fulfillment of the Requirements for the degree of

Master of Science in Biomedical Engineering



Weldon School of Biomedical Engineering

West Lafayette, Indiana

May 2020

**THE PURDUE UNIVERSITY GRADUATE SCHOOL
STATEMENT OF COMMITTEE APPROVAL**

Dr. Jacqueline Linnes, Chair

Weldon School of Biomedical Engineering

Dr. Steven Wereley

School of Mechanical Engineering

Dr. Sulma Mohammed

Department of Comparative Pathobiology

Dr. Tamara Kinzer-Ursem

Weldon School of Biomedical Engineering

Approved by:

Dr. George R. Wodicka

Dedicated to Barrett and Georgia

ACKNOWLEDGMENTS

First and foremost, thank you to all the members of my committee for your guidance and support throughout the past several years. Thank you to Dr. Linnes for three and a half years of amazing mentorship and advice in research, academic, professional, and personal realms. Thank you to Dr. Wereley for taking the time to help me develop new skills in an unfamiliar field and for many thoughtful, informed discussions and professional guidance. Thank you to Dr. Mohammed for the opportunity to take ownership of a unique project based on her previous work, and for all her help and guidance throughout. Finally, thank you to Dr. Kinzer-Ursem for her academic and professional guidance.

It is imperative that I thank Dr. Elizabeth Phillips, my graduate mentor from January 2017 – May 2019. Her guidance helped me develop my research and professional skills, and she inspired me to not only pursue research continuously throughout my undergraduate education, but also to extend my academic career into master's and, soon, Ph.D. studies.

The cervical cancer portion of this thesis began as a senior design project, and for that reason, I want to thank Sam Hawkins, Benjamin Moy, and Joseph Sawyer for taking the semester to help make the cervical cancer lateral flow assay idea into a tangible reality. Furthermore, thank you to Jessica Bendell, Barrett Davis, Haley June, and Sriram Malathi for jumping onboard for an additional semester to help with continued work on the project.

Thank you to my two undergraduate mentees, Lindsay Wright and Chase Rutan, for their help and insight in bringing the lateral flow assay from a proof-of-concept to an optimized, fully integrated device.

Thank you to Hui Ma and Jay Lee for helping me understand image processing and significantly expediting the PIV analysis process.

Finally, thank you very much to the Shah Family Global Innovation Lab for providing the necessary funding for me to pursue the cervical cancer lateral flow assay research, about which I am profoundly passionate, for my master's thesis, and for funding my travel to Kenya to participate in the African International Biotechnology and Biomedical Conference in August 2019. Thank you as well to the CTSI Women's Health fund for additional funding to permit continued development of this technology.

TABLE OF CONTENTS

LIST OF FIGURES	7
ABSTRACT.....	9
1. INTRODUCTION	10
2. LATERAL FLOW ASSAY DEVELOPMENT FOR EARLY CERVICAL CANCER DETECTION AT THE POINT OF CARE	13
2.1 Literature Review.....	13
2.2 Methods.....	15
2.2.1 Dot blots.....	15
Enzymatic detection	15
Gold nanoparticle detection	16
2.2.2 Lateral flow assay development	17
2.2.3 HeLa cell culture, preparation and detection	19
2.2.4 Lateral flow assay validation	19
2.3 Results.....	20
2.3.1 Dot blots.....	20
2.3.2 Lateral flow assays	24
2.4 Discussion.....	27
3. FLUIDIC CHARACTERIZATION OF LATERAL FLOW ASSAYS FOR EFFICIENT MULTI-STEP BIOMARKER DETECTION.....	33
3.1 Literature Review.....	33
3.2 Methods.....	35
3.2.1 Nitrocellulose properties and test strip construction	35
3.2.2 Scanning electron microscopy (SEM).....	35
3.2.3 Macroscopic imaging.....	36
3.2.4 Macroscopic analysis.....	36
3.2.5 Wax valve analysis	36
3.2.6 Microscopic imaging	37
3.2.7 Microscopic analysis	38
3.3 Results.....	39

3.3.1	Membrane homogeneity validation	39
3.3.2	Macroscopic flow analysis	40
3.3.3	Macroscopic flow modeling	41
3.3.4	Microscopic flow analysis	45
3.4	Discussion	46
4.	CONCLUSION.....	51
	APPENDIX A. CERVICAL CANCER.....	52
	APPENDIX B. MACRO AND MICROFLUIDIC ANALYSES.....	53
	REFERENCES	54

LIST OF FIGURES

Figure 1.1: Schematic of lateral flow assay construction, conceptual visualization of intrinsic biological properties, and method for interpreting results.	11
Figure 2.1: Schematic of lateral flow assay construction, conceptual visualization of intrinsic biological properties, and method for interpreting results.	18
Figure 2.2: A. Enzymatic dot blot showing binding of 10 $\mu\text{g/mL}$, 1 $\mu\text{g/mL}$, and 0.1 $\mu\text{g/mL}$ VCP to no primary antibody, 10 $\mu\text{g/mL}$ M15, and 10 $\mu\text{g/mL}$ M18. 1 mg/mL M15 is used as a positive control and 2 mg/mL biotinylated BSA is used as a negative control. B. Enzymatic dot blot showing binding of 100 $\mu\text{g/mL}$, 10 $\mu\text{g/mL}$, and 1 $\mu\text{g/mL}$ M15 and M18 to VCP and the opposite primary antibody in a sandwich assay. Positive and negative controls are identical to A. Contrast enhancement was performed using ImageJ (NIH) to adjust maximum and minimum gray values.	21
Figure 2.3: A. Dot blot with gold nanoparticles conjugated to only M18 incubated with 70 $\mu\text{g/mL}$, 10 $\mu\text{g/mL}$, and 1 $\mu\text{g/mL}$ VCP spots; the positive control is goat anti-mouse antibody and the negative control is 2 mg/mL biotinylated BSA. B. Dot blot with gold nanoparticles conjugated to both M18 and streptavidin poly-HRP. The left membrane was imaged prior to signal amplification; the right membrane was imaged after signal amplification with DAB. Test spots are the same as in A; the positive control is 2 mg/mL biotinylated BSA; the negative control is 2 mg/mL BSA. C. Sandwich assay dot blot with 1 mg/mL M15 as the test spot. Positive and negative controls are the same as in B.	23
Figure 2.4: HeLa cell enzymatic dot blots. Cells spots are dried at counts of 1×10^5 , 5×10^4 , 1×10^4 , 5×10^3 , and 1×10^3 cells.	24
Figure 2.5: A. Fully integrated lateral flow assays detecting purified VCP with dried gold nanoparticles conjugated to M18 only. B. Lateral flow assays detecting purified VCP run with double-conjugated gold nanoparticles in liquid form.	25
Figure 2.6: Validation of detection of purified VCP on fully integrated lateral flow assays at concentrations of A. 10 $\mu\text{g/mL}$, B. 5 $\mu\text{g/mL}$, C. 1 $\mu\text{g/mL}$, and D. 0.5 $\mu\text{g/mL}$ using E. 10 $\mu\text{g/mL}$ BSA as a negative control.	26
Figure 2.7: Validation of detection of lysed HeLa cells on fully integrated lateral flow assays at cell counts of A. 1×10^5 , B. 1×10^4 , C. 1×10^3 , and D. 1×10^2 using E. RIPA buffer only as a negative control.	27
Figure 2.8: Bar chart showing signal intensity contrast of test and control spots on lateral flow assays run with different HeLa cell counts. Error bars represent standard deviation ($n = 3$). The bar with a * (representing the control strips) is significantly smaller than the rest of the bars at $p < 0.20$ using a one-way ANOVA and Tukey's pairwise comparison ($p = 0.174$). <i>This is not technically statistically significant but that is likely due to the large variation in the signal intensity in the test strips; the control strips' test lines are clearly not visible to the human eye.</i>	27

Figure 3.1: **A.** Different valve geometries. **B.** Experimental setup for macroscopic flow analysis. 37

Figure 3.2: Diagram of microscope setup for imaging particle flow in nitrocellulose membrane 39

Figure 3.3: **A.** SEM image of surface of nitrocellulose membrane (1000X magnification). **B.** SEM image of cross-section of nitrocellulose membrane demonstrating homogeneity of pore structure throughout membrane depth (100X magnification). **C.** SEM image of cross-section of nitrocellulose membrane with wax melted throughout (1000X magnification). *Image courtesy of Elizabeth Phillips* **D.** Cryo-SEM of 400 nm green fluorescent nanoparticles (5000X magnification). **E.** Cryo-SEM of 400 nm green fluorescent nanoparticles in nitrocellulose membrane (5000X magnification). **F.** SEM of nitrocellulose membrane with wax melted throughout (5000X magnification). *Image courtesy of Elizabeth Phillips. Note: the white scale bar in the bottom right corner of each image represents 50 μm in Figures 3.3 A-C and 10 μm in Figures 3.3 D-F.* 40

Figure 3.4: **A.** Actuation time of medium valves (surface area = 5 mm²) of different geometries (n = 3 and error bars represent standard deviation). **B.** Rate of fluid flow past medium valves of different geometries compared to flow in unobstructed nitrocellulose (n = 3 and error bars represent standard error of mean). 41

Figure 3.5: Macroscopic fluid velocity in the left, middle, and right of the nitrocellulose membrane past **A.** straight, **B.** concave, and **C.** convex valves. Error bars represent standard error of the mean (n = 3). 42

Figure 3.6: Mathematical model describing flow in nitrocellulose membranes. **A.** The macroscopic flow rate unobstructed by wax valves (unitless distance and time). **B.** Flow pattern along nitrocellulose membrane at equally spaced time points past valves of different geometries. **C.** Flow rates past different valve geometries. *Images produced by Hui Ma.* 45

Figure 3.7: **Left:** All 400 images from a 10 second time series taken 15 mm from the sample pad in the center of the membrane combined into a single image to display locations of visible particles, with an overlaying vector field from EDPIV analysis (red arrows; green arrow represents the length of a 1 mm/s velocity vector in both the x and y directions). **Right:** Histogram reflecting the velocity distribution of all 225 vectors in this analysis. 46

Figure 4.1: Dot blots comparing signal intensity from binding of M15 with HeLa cells and purified VCP to back-calculate protein concentration per cell count based on signal. 52

ABSTRACT

Paper-fluidic devices are a popular platform for point-of-care diagnostics due to their low cost, ease of use, and equipment-free detection of target molecules. The most common example is the lateral flow assay, in which samples are added to a paper membrane and a colorimetric indicator provides a binary signal indicating whether the molecule of interest is present. A novel lateral flow assay was developed to detect a protein biomarker for early stage cervical cancer. Cervical cancer can be cured if detected and treated at an early stage, but approximately 90% of cervical cancer deaths occur in low and middle-income countries due to lack of accessible testing. Methods for detecting the biomarker, valosin-containing protein (VCP), were optimized using enzymatic and gold nanoparticle dot blots, then lateral flow assays were developed and validated using purified VCP and cervical cancer HeLa cells. Future validation with patient tissue samples will permit translation of this device to testing clinics in low-resource areas.

Despite advantages for use in resource limited settings, lateral flow assays are limited by their inability to perform more complex or multi-step processes, such as nucleic acid amplification or enzymatic signal enhancement. Thermally actuated wax valves are one mechanism that provides complete control over fluid obstruction and release. To better understand how wax valves can be used in fully automated, self-contained lateral flow assays, different sizes and geometries of valves were tested to investigate their effects on actuation time, flow rate, and flow pattern. Another limitation in the understanding of lateral flow assays is the lack of experimental data describing the microscale flow within the pores of the paper membrane that drives the biophysical reactions in the assay. Mathematical models can be designed to explain macroscopic phenomena, but so far, no literature has compared microfluidic models to microfluidic data. To quantify microfluidic properties within lateral flow assays, fluorescent nanoparticles were imaged flowing through different areas of the membrane and their velocity was quantified using micro-particle image velocimetry (μ PIV). Scanning electron microscope images were used to verify that this experimental model was reasonable for describing microfluidic properties of the lateral flow assay. Altogether, this document investigates how developing lateral flow assays for cervical cancer detection can save lives by improving the accessibility of an early diagnosis, and how more robust lateral flow assay characterization can expand their applicability to a broad range of detection processes.

1. INTRODUCTION

Since the invention of the one-step home pregnancy test in the 1980s¹, lateral flow assays (LFAs) have become increasingly popular for on-demand testing and detection. While the home pregnancy test arguably remains the most widely known example, LFAs have been developed for everyday use for a variety of medical and environmental applications. Today, LFAs are an extensively used platform for point-of-care diagnostics due to their low-cost implementation in remote and resource-limited settings.² Capillary action drives a deposited sample through a conventional LFA for colorimetric analysis, circumventing the pumps typically required for small molecule detection.³ This equipment-free analysis makes LFAs an ideal platform for the rapid screening of a broad spectrum of environmental and biological analytes.⁴ From rapid *Streptococcus* testing in local clinics to recent developments in malaria and HIV testing, LFAs are rapid, low-cost, easy-to-use tests that nearly anyone can perform without additional equipment.

A basic lateral flow immunoassay using gold nanoparticles (GNPs) as a colorimetric indicator is shown in Figure 1.1. First, a liquid sample containing an analyte of interest is first added to an adsorbent sample pad (1). The sample then flows to a GNP conjugate pad (2), where GNPs bound to antibodies specific to the analyte have been dried into glass fiber. Any analyte present in the sample will bind to these GNPs and the liquid from the sample will release the GNPs, allowing them to flow through the nitrocellulose membrane, where there are two detection zones: first, a test line (3), where different antibodies specific to the analyte have been dried, and then a control line (4), where a substance has been dried that will bind to the antibodies on the GNPs. If the analyte is present and bound to the GNPs, they will aggregate along the test line, forming a visible red line. Whether the analyte is present or not, any remaining GNPs that have not bound to the test line will bind to the control line to prove validity of the test. Finally, any remaining liquid from the sample will be absorbed by an absorbent pad at the end of the nitrocellulose membrane.⁵

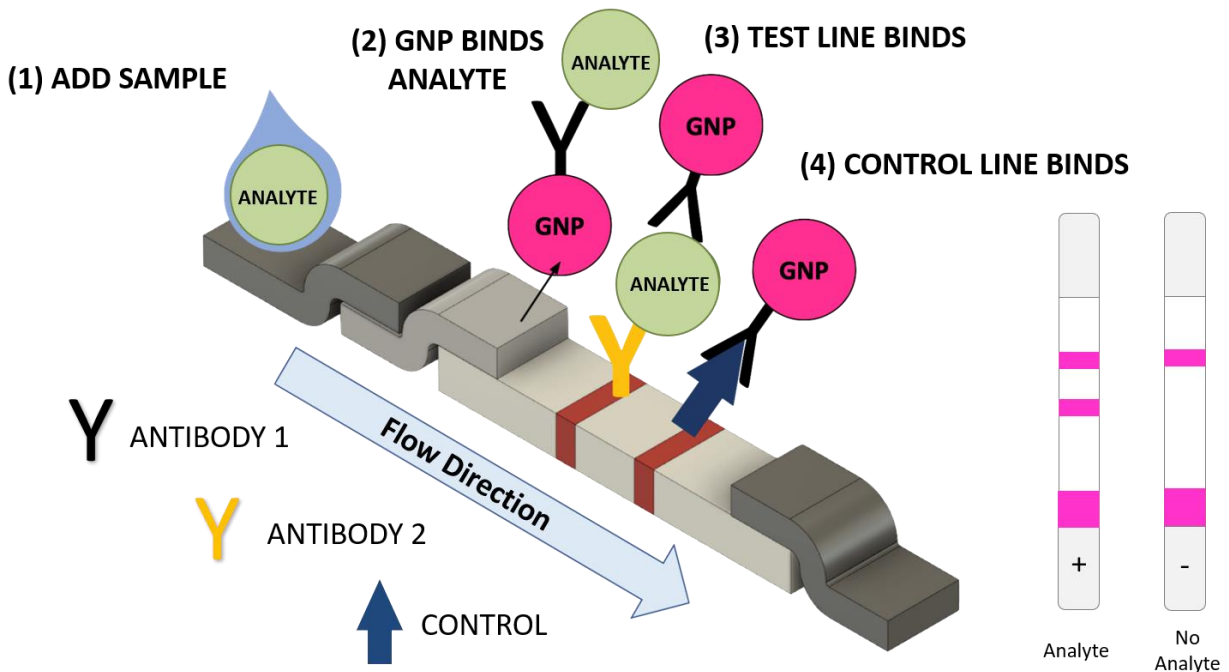


Figure 1.1: Schematic of lateral flow assay construction, conceptual visualization of intrinsic biological properties, and method for interpreting results.

Widespread use of LFAs is limited, especially in developed countries, because their sensitivity and specificity are insufficient compared to gold-standard laboratory procedures.⁶ Without technologies that are compatible with their available resources, however, resource-limited clinics must struggle with lack of infrastructure of trying to access distant facilities or are simply not able to perform testing at all. The limitations of current point-of-care detection technologies do not negate the need for them in resource-limited settings. Thus, Chapter 2, I describe my development of an LFA for biomarker detection of cervical cancer, a disease that disproportionately affects women in low-resource areas due to lack of access to timely and accurate testing and treatment.

One of the primary reasons for the limited accuracy of LFAs is that sensitive detection requires sufficient binding time between the analyte in the sample and the reagents in the paper membrane, which is difficult to achieve when timing is dictated by capillary flow rate.⁷ Additionally, unprocessed bodily fluids, which are frequently used in point-of-care testing, are complex and contain components that inhibit detection or obscure colorimetric results.⁸ The lack of sample filtration and signal amplification causes high rates of false positive or false negative

LFA results.⁹ Moreover, LFAs provide only semi-quantitative results of analyte concentration, requiring follow-up analysis.⁸ To achieve sensitive and specific analyte detection required to inform clinical decisions, conventional LFAs are painstakingly engineered and optimized for each analyte of interest.⁹

As useful as lateral flow assays have proven to be for some applications, many forms of biomolecule detection require more complex processes than can currently be incorporated in a simple paper test strip, which is another major limitation to their widespread implementation in clinics with a range of resource levels. Processes such as pathogen detection or the identification of very small amounts of a molecule require amplification of the signal, either by increasing the copies of a nucleic acid or using enzymatic reactions to improve the visibility of the relevant reaction. Because these processes require multiple steps, they eliminate the main advantage of the LFA: its capacity to be performed with a single user step and in an equipment-free setting.

If lateral flow assays were more sensitive and specific and capable of performing more complex detection processes, their scope would be greatly expanded, and they could be implemented for a variety of applications in both high and low-resource settings. One of the main limitations to innovating these next-generation LFAs, however, is our lack of fundamental experimental data that describes how and why they work the way they do. Conceptually, we know that lateral flow assays pull samples through them with capillary action and that affinities of molecules for each other constitute the relevant bioreactions that produce readable results, but a robust analysis at both the macroscale and microscale is lacking from the field of assay development and characterization. In Chapter 3, I describe characterization of thermally actuated wax valves, a fluidic control method for multi-step LFAs developed by Dr. Elizabeth Phillips, a former graduate student in the Linnes Lab at Purdue, that I have optimized for more precise implementation. I also describe how mathematical models can be used to describe some of the counterintuitive observations made when characterizing these valves, and how scanning electron microscope images can be used to validate the underlying assumptions behind these models. Finally, I introduce an entirely novel method of visualizing and quantifying particle motion within LFAs, permitting precise characterization of the microscale fluid behavior and biophysical reactions behind them, elucidating how LFAs work. Altogether, an improved, evidence-based understanding of lateral flow assays will permit more efficient and intelligent development of novel devices for point-of-care detection.

2. LATERAL FLOW ASSAY DEVELOPMENT FOR EARLY CERVICAL CANCER DETECTION AT THE POINT OF CARE

2.1 Literature Review

Cervical cancer is the leading cause of cancer death in sub-Saharan Africa,¹⁰ with an average age-standardized incidence rate of invasive cervical cancer of 43.1 cases per 100,000 women.¹¹ Comparatively, countries with high Human Development Index had an average incidence rate of 9.6 cases per 100,000 women.¹¹ Because cervical cancer can be effectively treated and cured if diagnosed at an early stage, this discrepancy in patient outcomes is largely due to the availability and success of screening programs in different regions. Regular screening is associated with a 67% reduction in stage 1A cancer and a 95% reduction in stage 3 or worse cancer,¹² however, only 5% of women in developing countries are screened compared to 40-50% of women in developed countries.¹⁰ In high-resource areas, cytologic screening programs that utilize the Pap smear have been successfully implemented, leading to a reduction in incidences. For example, widespread Pap screening in the United States beginning in the early 1950s resulted in a massive decline in cervical cancer incidence and mortality by referring patients for treatment at very early stages.¹³ This method, however, requires advanced infrastructure including an established laboratory, highly trained cytologists, and multiple patient visits for follow-up screening and treatment that make it very infeasible for areas with limited resources.¹⁴ Furthermore, when clinics in these areas do implement Pap smear screenings, they are not sufficiently effective; one study of 13 clinics in Mexico city found a false negative rate of as high as 54%.¹⁰ For this reason, in low-resource settings, patients are often not diagnosed until they have symptomatic presentations,¹⁵ at which point the disease has already progressed to a more advanced stage¹⁶ with a lower chance of survival. Ultimately, nearly 90% of cervical cancer deaths occur in low and middle-income countries due to the lack of access to screening and timely diagnosis and treatment.¹⁷

A variety of point-of-care screening methods have been developed and implemented to improve the accessibility of a timely diagnosis to patients in low-resource areas. One successfully implemented measure is visual inspection with acetic acid (VIA). In this method, 5% acetic acid is applied to the cervix, causing low-grade cervical intraepithelial neoplasia (CIN I) lesions to turn a pale white color, and high-grade (CIN II-III) lesions to turn a dense white color with sharp borders.¹⁸ One study found this method to successfully detect 15% more abnormal cases than

cytological methods.¹⁹ A similar method can also be employed using Lugol's iodine (VILI), which has a similar sensitivity to and higher specificity than VIA.²⁰ Combining VIA and VILI has been shown to result in 94.7% sensitivity. These tests, however, have low specificity and result in false-positive results,²¹ sometimes leading to overtreatment.²²

Another alternative method to cytological screening for cervical cancer involves testing for human papillomavirus (HPV), a sexually transmitted infection responsible for most cervical cancers.²³ Approximately 80 percent of people will contract some form of HPV at some point in their lives;²⁴ however, there are over 100 HPV genotypes, 12 of which are oncogenic, two of which (types 16 and 18) are associated with 70% of cervical cancer cases.²⁵ Many point-of-care tests for HPV have been developed in recent years and have been evaluated as more sensitive than cytology, but tend to have a lower specificity, especially in high HPV prevalence populations such as women living with HIV.^{26,27} Additionally, most HPV infections are cleared naturally,²⁸ and those that do result in cervical cancer take many years to reach that point.²⁹ Due to the high prevalence of HPV infection in the absence of cervical cancer, routine screening for HPV has not been recommended in the past,³⁰ and continue to be controversial in extremely resource-limited areas where allocation of treatment to patients who most need it is essential. HPV testing must be coupled with a triage system for follow-up cancer screening and requires multiple visits for testing and treatment, resulting in loss of patients to follow-up.¹⁴

Briefly, within the past decade, several novel technologies utilizing machine learning or advanced imaging techniques have emerged as potential methods for expediting and simplifying an accurate cervical cancer diagnosis, including the use of machine learning to automatically evaluate pap smear images and a high-resolution microendoscope with image analysis software to interrogate cells on the surface of the cervix.^{31,32} Both techniques, however, are still emerging and are limited by their needs for further validation and training of personnel in resource-limited settings.

The most effective cervical cancer test would permit healthcare workers to reach patients in rural and resource-limited settings and identify those with possible early-stage cancer to refer them for treatment. The recent identification of several protein biomarkers offers the potential development of immunological detection methods. Immunological detection can easily be incorporated in paper-based detection methods like a lateral flow assay for use at the point of care. One specific protein identified to indicate late-stage CIN and early stage cancer is valosin-

containing protein (VCP).³³ Here, we develop a method for detecting VCP from cervical cancer cells that is entirely equipment-free, and discuss necessary future steps for validation of this method and its implementation in cervical cancer screening programs in low-resource areas.

2.2 Methods

2.2.1 Dot blots

Dot blots³⁴⁻³⁶ were used to confirm binding of the detection and capture anti-VCP antibodies (M18 and M15 - Abnova) used in previous cervical cancer protein biomarker detection³³ to purified VCP and cervical cancer HeLa cells. Enzymatic detection methods were first used to verify individual binding and binding in a sandwich format, then gold nanoparticles were conjugated to both antibodies to verify their potential use as a colorimetric detection method that could be integrated into a lateral flow assay.

Enzymatic detection

To verify effective binding of both M15 and M18 to VCP, VCP (Abnova) was diluted in 1X Tris-buffered saline (TBS) to concentrations of 10 $\mu\text{g/mL}$, 1 $\mu\text{g/mL}$, and 0.1 $\mu\text{g/mL}$. 1 μL of each solution was spotted on two different FF120 nitrocellulose membranes (GE Healthcare) and permitted to dry. 1 μL of 1 mg/mL M15 was used as a positive control, and 1 μL of 2 mg/mL biotinylated BSA was used as a negative control. Once both membranes were dry, they were blocked in a solution of 5% bovine serum albumin (BSA) in TBS supplemented with 0.05% Tween-20 (TBST – the entire solution will from this point forward be abbreviated as BSA-TBST) by adding each strip to a 2 mL Eppendorf tube containing 1 mL BSA-TBST and rotating the tube for 1 hour at room temperature.

Next, the primary antibodies, M15 and M18, were each diluted to a final concentration of 10 $\mu\text{g/mL}$ in 1 mL BSA-TBST in 2 mL Eppendorf tubes. The blocking solution was poured off each membrane, and one membrane was added to each tube. These tubes were rotated for 2 hours at room temperature to allow the primary antibody sufficient incubation time in contact with the dried VCP. Following incubation with the primary antibody, each membrane was washed three times in TBST for 5 minutes each time.

Next, the secondary antibody, goat anti-mouse with a horseradish peroxidase (HRP) tag, was diluted to a final concentration of 10 $\mu\text{g}/\text{mL}$ in 1 mL BSA-TBST per 2 mL Eppendorf tube. After washing, each membrane was placed in a tube and spun for 2 hours to allow sufficient time for incubation with the secondary antibody. After incubation, both membranes were washed in TBST for 15 minutes one time and 5 minutes twice and were then washed in TBS for 5 minutes.

Following the final wash step, membranes were placed in a petri dish and tetramethylbenzidine (TMB) substrate, which reacts with HRP to produce a colorimetric signal, was poured into the petri dish so the membranes were completely submerged. The resulting signal developed for 10 minutes, after which the membranes were removed from the TMB and imaged. Then, the membranes were washed in TBS to stop the enzymatic reaction and imaged again. Membranes were imaged a final time once completely dry. ImageJ (NIH) was used to calculate the intensity of the signals produced in these dot blots.

Gold nanoparticle detection

Once binding was confirmed with an enzymatic reaction, gold nanoparticles were used to validate their ability to be conjugated to a detection antibody and bind to a dried protein on paper. First, a single conjugation was performed with binding of the detection antibody only to 40 nm *N*-hydroxysuccinimide (NHS)-activated gold nanoparticles (Cytodiagnosics).³⁷ This procedure was done using both M15 and M18 as detection antibodies at different times. First, the detection antibody was diluted to a final concentration of 0.5 mg/mL using the supplied protein resuspension buffer. Then, 24 μL of the antibody solution was mixed with 84 μL of the supplied reaction buffer. 90 μL of this solution was transferred to a vial containing lyophilized NHS-activated gold nanoparticles, which were resuspended by pipetting the solution up and down. The resulting gold nanoparticle solution was incubated at room temperature for 2 hours, after which 10 μL of supplied quencher solution was added to the vial to stop the reaction along with 10 μL of 10% BSA. Then, the vial was centrifuged for 30 minutes at $1,400 \times g$. The supernatant containing the unbound protein was removed, and 100 μL of gold nanoparticle storage buffer (10% sucrose, 1% Tween-20, 0.5% BSA, 0.2% polyethylene glycol (PEG), 0.5% polyvinylpyrrolidone (PVP) in 1X phosphate-buffered saline (PBS)) was used to resuspend the conjugated gold nanoparticles. This nanoparticle solution could be stored at 4°C for up to 3 days before use.

Subsequent experiments required that the gold nanoparticles be conjugated to both the detection antibody and a second antibody, streptavidin poly-HRP in a procedure referred to here as double conjugation. For the double conjugation, first, the detection antibody was added to 1 mL of gold nanoparticles (plain, non-NHS-activated) for a final antibody concentration of 10 $\mu\text{g/mL}$. This solution was rotated for 1 hour. Then, streptavidin poly-HRP was diluted in the solution to a final concentration of 10 $\mu\text{g/mL}$, and the entire solution was rotated overnight to incubate. Following incubation, first, 10 mg BSA Fraction V was added to the tube and rotated for 1 hour. Then, 2 mg PEG was added to the tube and rotated for 1 hour. The tube was then centrifuged for 30 minutes at $2,500 \times g$, after which the supernatant was discarded, and the same gold pre-buffer solution used with the NHS-activated gold nanoparticles was used to resuspend the conjugated gold nanoparticle pellet. This solution could be stored at 4°C for up to 2 days before use.

Dot blots with the gold nanoparticles were performed using the same methods described for the enzymatic dot blots, except the gold nanoparticles replaced the primary antibody for incubation and were permitted to incubate overnight. The membranes were imaged immediately following this incubation; no secondary antibody was necessary because the gold nanoparticles themselves served as the colorimetric indicator. For the double-conjugated gold nanoparticles, subsequent enzymatic signal amplification was performed by adding 1 tablet diaminobenzidine (DAB) and 1 tablet HRP to 1 mL deionized water and letting the membranes incubate in this solution for 1 hour, after which they were washed in PBS supplemented with 0.05% Tween-20 (PBST) and imaged again. ImageJ was also used to quantify the signal intensity of these dot blots.

2.2.2 Lateral flow assay development

Lateral flow assays were designed and constructed to detect VCP in a single step as shown in Figure 2.1. Test and control spots were deposited on a $0.5 \text{ cm} \times 2.5 \text{ cm}$ FF120 HP nitrocellulose membrane by spotting 1 μL of 1 mg/mL M15 and 1 μL of goat anti-mouse antibody, respectively, on the membrane. The test and control spots were placed 1.25 cm and 1.75 cm from the sample end of the membrane, respectively. Once dry, the membranes were blocked in 5% sucrose, 2% BSA, 0.25% PVP, and 0.05% Tween-20 in 1X PBS for 1 hour, then left to dry overnight at room temperature.

Conjugated gold nanoparticles were diluted to various extents in the gold pre-buffer solution and pipetted onto 0.5×0.5 cm glass fiber pads (Millpore) in a petri dish at $12.5 \mu\text{L}$ per pad. The petri dishes were placed in a 37°C incubator overnight to dry the gold nanoparticles. To assemble the lateral flow assays, the nitrocellulose membranes were placed on a sticky backing card. If they were being tested with the dried gold nanoparticle pads, these were then placed at the sample end of the strip, overlapping it by 1 mm. Then, the sample pad, a $1 \text{ cm} \times 0.5 \text{ cm}$ glass fiber pad, was placed on top of the gold nanoparticle pad, overlapping it by 1 mm. Finally, the collection pad, an approximately $3 \text{ cm} \times 0.5 \text{ cm}$ cellulose pad was placed at the opposite end of the nitrocellulose membrane from the sample and gold nanoparticle pads, overlapping the membrane by 1 mm. Firm contact was ensured between all components of the lateral flow assays.

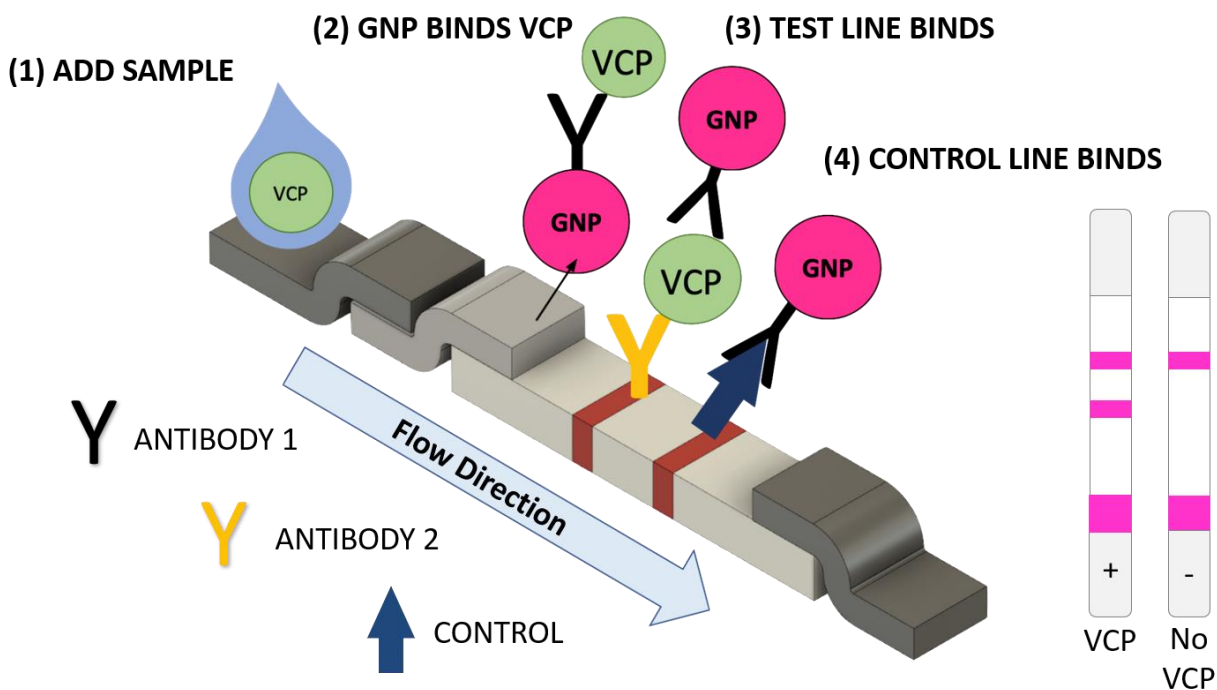


Figure 2.1: Schematic of lateral flow assay construction, conceptual visualization of intrinsic biological properties, and method for interpreting results.

2.2.3 HeLa cell culture, preparation and detection

HeLa cells were cultured in Eagle's Minimum Essential Medium (EMEM) supplemented with 10% FBS. Cells were split upon reaching 75-90% confluency using trypsinization and resuspension. To harvest cells, 1.5 mL trypsin was added to each flask; then, an additional 3.5 mL EMEM was added to resuspend the detached cells. 5 mL of the cell-containing media was transferred to a 15 mL conical tube and centrifuged at $500 \times g$ for 5 minutes. The supernatant was discarded, and the pelleted cells were resuspended in 1 mL media. Cells from this suspension were counted using a LUNA-FL Dual Fluorescence Cell Counter (Logos Biosystems).

Because VCP is a cytosolic protein,³⁸ once harvested and counted, cells were spun down in a microcentrifuge and resuspended in 0.5 mL RIPA buffer (1 M sodium chloride, 1% Nonidet P-40, 0.5% sodium deoxycholate (DOC), 0.1% sodium dodecyl sulfate (SDS), and 50 mM Tris, pH 7.4 in double distilled water) for approximately every 5×10^6 cells.³⁹ The solution was agitated by hand before use to homogenize the contents.

Enzymatic dot blots were performed to detect VCP from cell lysate using the procedure described in Section 3.2.1.1. Approximate cell counts were calculated according to the corresponding necessary volume of lysate.

2.2.4 Lateral flow assay validation

Lateral flow assay efficacy was validated at different points in the development process. For tests run without dried nanoparticles, test strips were constructed without the gold nanoparticle pad and relevant concentrations of VCP were diluted in 40 μ L of gold nanoparticle solution and pipetted directly onto the sample pad of the assay. For tests run with dried nanoparticles, relevant concentrations of VCP and HeLa cell lysate were diluted in 40 μ L of 1X PBS and added to the sample pad with a pipette. For VCP assays, 10 μ g/mL BSA in 1X PBS was used as a negative control; for the HeLa cell assays, plain RIPA buffer served as the negative control. Test strips were given 15 minutes to run before being imaged for subsequent signal intensity analysis.

2.3 Results

2.3.1 Dot blots

Before lateral flow assay development, dot blots were performed to verify and optimize functionality of their constituent components. First, enzymatic dot blots were performed to test whether both anti-VCP antibodies (M15 and M18) bound to VCP exclusively, and at what sensitivity. In the first of these tests, VCP was dried directly on the nitrocellulose membrane in a serial dilution of 10 $\mu\text{g/mL}$, 1 $\mu\text{g/mL}$, and 0.1 $\mu\text{g/mL}$. 1 mg/mL M15 was used as a positive control because, as a mouse antibody, the anti-mouse secondary antibody with the HRP tag was guaranteed to bind to it and produce a signal. 2 mg/mL biotinylated BSA was used as a negative control. In addition to testing for M15 and M18 binding, a dot blot was run on a separate strip with the same VCP, positive control, and negative control spots but without a primary antibody to test for nonspecific binding of the secondary antibody.

As shown in Figure 2.2A, incubating the membranes in both M15 and M18 resulting in a very strong binding signal to the 10 $\mu\text{g/mL}$ spot. A fainter, but still visible binding signal, was also observed for the 1 $\mu\text{g/mL}$ spot, while no visible signal was discernable for the 0.1 $\mu\text{g/mL}$ spot. The strong positive control signal and indiscernible negative control spot validated sensitivity of both the primary and secondary antibodies to their respective binding targets. It is worth noting that in the absence of incubation with a primary antibody, a faint binding signal was still observed for the 10 $\mu\text{g/mL}$ VCP spot. This indicates that some nonspecific binding occurred between the secondary (anti-mouse) antibody and VCP.

Following validation of binding between the individual antibodies and VCP, a dot blot was performed in a sandwich format to test the feasibility of this assay for implementation in a lateral flow assay. Both possible formats were tested; that is, both M18 and M15 were used as the capture (dried on paper) and detection (used for incubation after VCP binding) antibodies. Both antibodies were dried onto nitrocellulose membranes at concentrations of 100 $\mu\text{g/mL}$, 10 $\mu\text{g/mL}$, and 1 $\mu\text{g/mL}$. The same positive and negative controls as described previously were used. Once the membranes were prepared, both were incubated with 5 $\mu\text{g/mL}$ VCP, then 10 $\mu\text{g/mL}$ of the opposite antibody to the one dried on the membrane. After both incubation steps, membranes were incubated with the HRP-tagged secondary antibody and the visible signal was produced. As shown in Figure 2.2B with enhanced image contrast, when M15 was used as the capture antibody, binding

signal was visible at both 100 $\mu\text{g/mL}$ and 10 $\mu\text{g/mL}$ antibody spots. When M18 was used as the capture antibody, binding signal was visible at 100 $\mu\text{g/mL}$, although this signal was weaker than that of the M15 antibody at the same concentration. As before, strong signal was visible for the positive control and signal was absent from the negative control. These results verified the possibility of constructing a sandwich-format lateral flow assay and informed the decision to use M15 as the capture antibody and M18 as the detection antibody.

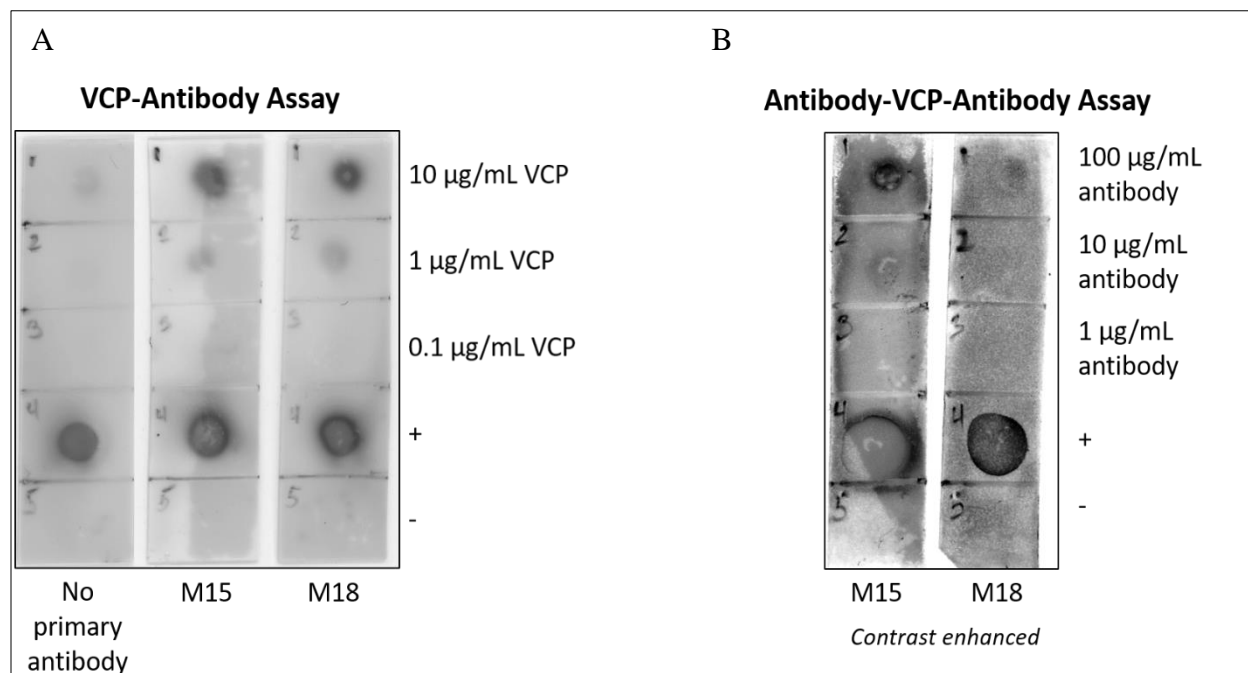


Figure 2.2: **A.** Enzymatic dot blot showing binding of 10 $\mu\text{g/mL}$, 1 $\mu\text{g/mL}$, and 0.1 $\mu\text{g/mL}$ VCP to no primary antibody, 10 $\mu\text{g/mL}$ M15, and 10 $\mu\text{g/mL}$ M18. 1 mg/mL M15 is used as a positive control and 2 mg/mL biotinylated BSA is used as a negative control. **B.** Enzymatic dot blot showing binding of 100 $\mu\text{g/mL}$, 10 $\mu\text{g/mL}$, and 1 $\mu\text{g/mL}$ M15 and M18 to VCP and the opposite primary antibody in a sandwich assay. Positive and negative controls are identical to A. Contrast enhancement was performed using ImageJ (NIH) to adjust maximum and minimum gray values.

Once the protein was effectively detected on a dot blot using an enzyme-based signal, gold nanoparticles were conjugated to M18, the detection antibody, and the dot blot was repeated using the conjugated gold nanoparticles in place of the individual primary and tagged secondary antibodies with an enzymatic signal. As shown in Figure 2.3A, this dot blot resulted in a faint binding signal produced by the gold nanoparticles binding to the 70 $\mu\text{g/mL}$ VCP spot and a strong signal from the gold nanoparticles binding to the positive control spot.

Due to the weak signal produced by binding of the gold nanoparticles to a very high concentration of VCP, the implementation of enzymatic signal enhancement was investigated to

produce a more visible signal after nanoparticle binding. To do this, gold nanoparticles were conjugated to both M18 and streptavidin poly-HRP. Once conjugated, the gold nanoparticle dot blot was performed again. After the initial incubation of the membranes with the gold nanoparticles, the membranes were incubated in a solution containing DAB and hydrogen peroxide. The HRP enzyme reacted with the DAB, oxidizing it and causing it to produce a dark brown color in the presence of HRP (where the HRP-tagged gold nanoparticles were bound). Figure 2.3B shows the results of this experiment. Interestingly, prior to signal enhancement with DAB, the nanoparticles double-conjugated to both M18 and streptavidin poly-HRP produced much stronger binding signals to all three VCP concentrations, with clearly visible signal at both the 70 $\mu\text{g/mL}$ and 10 $\mu\text{g/mL}$ spots. For these dot blots, biotinylated BSA was used as the positive control because streptavidin was expected to bind to biotin with a very high affinity. The signal produced at the positive control spot here, however, was much fainter than when goat anti-mouse was used as the positive control; signal was not observed until after enzymatic amplification. Enzymatic amplification did slightly increase the signal intensity of the 70 $\mu\text{g/mL}$ and 10 $\mu\text{g/mL}$ spots, but not to an extent that would make them much easier to read than the non-amplified signal. Based on these observations, in developing the lateral flow assays, goat anti-mouse was used as the control spot, and gold nanoparticles were conjugated to both M18 and streptavidin poly-HRP. For the sake of simplicity, enzymatic signal amplification was not implemented in early designs, but the production of the gold nanoparticles allows this to be an option should future developments require it.

As a final verification step prior to lateral flow assay development, the gold nanoparticle dot blots were performed in a sandwich format. For these dot blots, 1 mg/mL M15 was dried on the nitrocellulose membrane, which was then incubated in 10 $\mu\text{g/mL}$ VCP prior to incubation with the double-conjugated gold nanoparticles. The membranes were imaged after this incubation step, and then incubated in solution with DAB and hydrogen peroxide for signal amplification and imaged again. The signal produced here was very faint on the M15 spot only, and as in previous experiments, enzymatic amplification did not significantly increase the readability of the signal. Still; this dot blot verified the proof-of-concept that protein detection in a sandwich format could be implemented into a lateral flow assay using conjugated gold nanoparticles to produce a colorimetric signal.

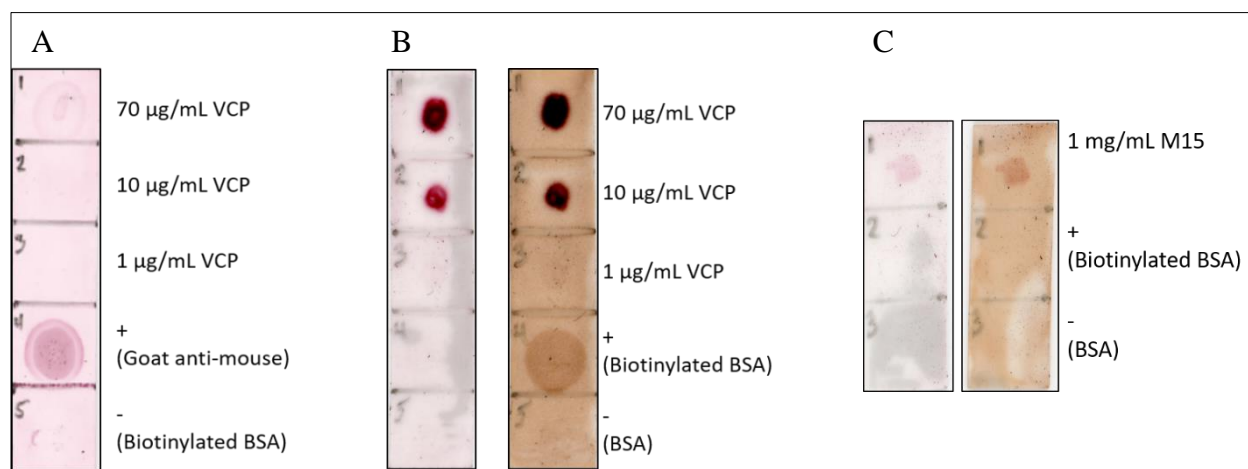


Figure 2.3: **A.** Dot blot with gold nanoparticles conjugated to only M18 incubated with 70 $\mu\text{g/mL}$, 10 $\mu\text{g/mL}$, and 1 $\mu\text{g/mL}$ VCP spots; the positive control is goat anti-mouse antibody and the negative control is 2 mg/mL biotinylated BSA. **B.** Dot blot with gold nanoparticles conjugated to both M18 and streptavidin poly-HRP. The left membrane was imaged prior to signal amplification; the right membrane was imaged after signal amplification with DAB. Test spots are the same as in A; the positive control is 2 mg/mL biotinylated BSA; the negative control is 2 mg/mL BSA. **C.** Sandwich assay dot blot with 1 mg/mL M15 as the test spot. Positive and negative controls are the same as in B.

Following confirmation of antibody binding to purified VCP, cervical cancer HeLa cells were cultured, harvested, and counted to test whether VCP, a cytosolic protein, could be detected from whole cell samples. After harvested cells were counted, they were centrifuged to remove extra media and resuspended in 0.5 mL RIPA buffer for every 5×10^6 cells to lyse the cells. Lysed cells were spotted on nitrocellulose membranes at cell counts of 1×10^5 , 5×10^4 , 1×10^4 , 5×10^3 , and 1×10^3 . An enzymatic dot blot was then performed using M15 as the primary antibody and HRP-tagged goat-anti-mouse as the secondary antibody, using TMB to produce a colorimetric signal.

As shown in Figure 2.4, strong signal was visible for all 5 cell counts, with the most intense signal for 1×10^5 cells, and the signal decreasing slightly with successive cell dilutions, but not to an extent that limited signal readability. This experiment validated that VCP could be detected from HeLa cells lysed with a room-temperature buffer and equipment-free processing (note: centrifugation was only used to remove media, which would not be present in human tissue samples or cervical swabs).

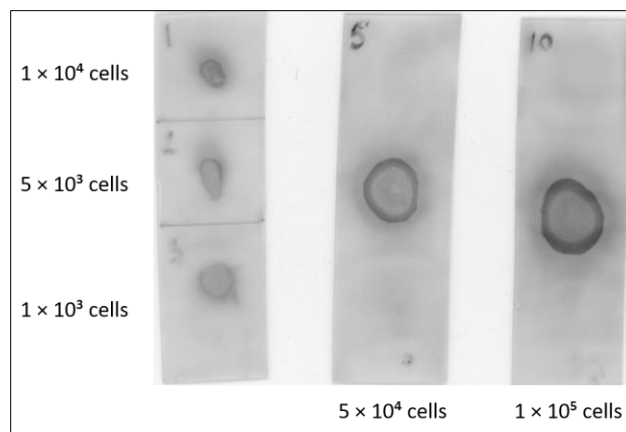


Figure 2.4: HeLa cell enzymatic dot blots. Cells spots are dried at counts of 1×10^5 , 5×10^4 , 1×10^4 , 5×10^3 , and 1×10^3 cells.

2.3.2 Lateral flow assays

Lateral flow assays were constructed and tested during various iterations of the gold nanoparticle conjugation and preparation process. Figure 2.5A shows an early attempt at constructing and testing a fully integrated lateral flow assay. Here, nanoparticles conjugated only to M18 were dried on a glass fiber pad, which was placed on top of a nitrocellulose test strip. On the nitrocellulose membrane, 1 mg/mL M15 served as the test spot, and goat-anti-mouse served as the control spot. In this test, the positive sample was run by adding 2 μ L stock VCP (70 μ g/mL) to the sample pad followed by 40 μ L PBS. The negative control was simply 40 μ L PBS added to the sample pad. With digitally enhanced contrast, here, it is possible to see an extremely faint test spot for the positive sample, and no test spot for the negative sample, with strong control spots on both assays. This indicates that the conjugated gold nanoparticles retained their integrity during the drying and rehydration process; however, the faint test spot was not nearly visible enough to be easily discernible from a negative sample with the naked eye, further informing the need for an improved design suggested by the single-conjugation dot blot results.

Figure 2.5B shows an early iteration of a lateral flow assay in which gold nanoparticles conjugated to both M18 and streptavidin-poly-HRP were used. Unlike the test run in Figure 2.5A, these nanoparticles were not dried down; instead, VCP was diluted directly in the gold nanoparticle solution to a concentration of 10 μ g/mL. 40 μ L of this solution was then added to the sample pad. In Figure 2.5B, it is very apparent that the double-conjugated nanoparticles produced a far stronger

signal at the test line than the single-conjugated nanoparticles. Here, both the test and control lines are clearly visible to the naked eye and do not require digital enhancement to read.

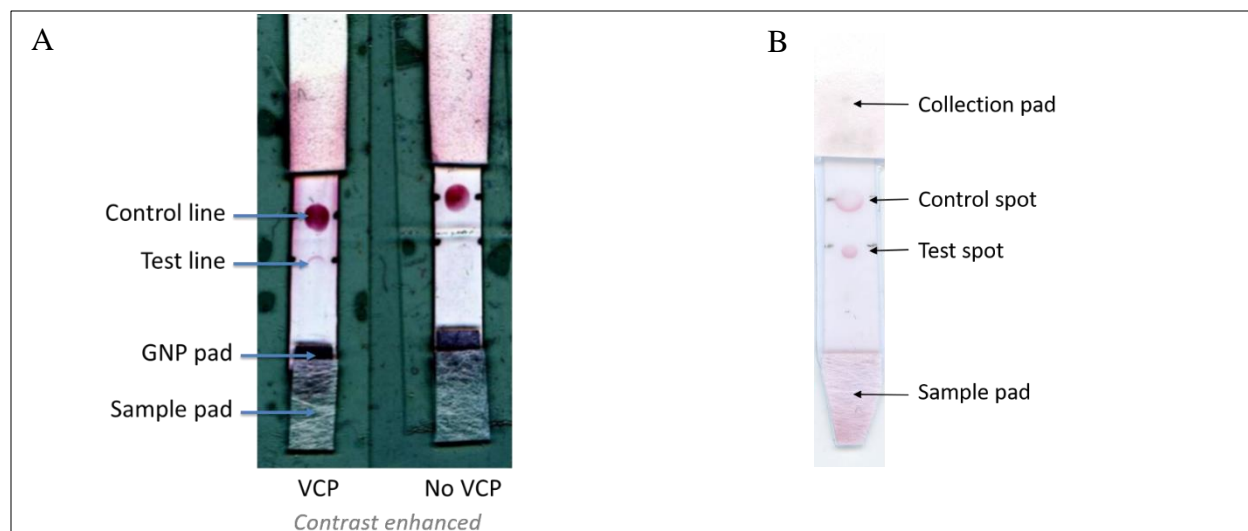


Figure 2.5: **A.** Fully integrated lateral flow assays detecting purified VCP with dried gold nanoparticles conjugated to M18 only. **B.** Lateral flow assays detecting purified VCP run with double-conjugated gold nanoparticles in liquid form.

After early iterations in the lateral flow assay development process led to the successful detection of VCP with double-conjugated nanoparticles in liquid form, those nanoparticles were dried onto glass fiber pads for stability after storage exceeding 2 days post-conjugation. After an optimal drying buffer and protocol were determined, it was possible to construct a fully integrated lateral flow assay with dried, double-conjugated gold nanoparticles. Next, the lateral flow assays were validated to determine the lower limit of detection of purified VCP. To do this, 10 $\mu\text{g/mL}$, 5 $\mu\text{g/mL}$, 1 $\mu\text{g/mL}$, and 0.5 $\mu\text{g/mL}$ VCP solutions were made by diluting the protein in 1X PBS. 40 μL of each solution ($n = 3$) was added to the sample pad of each lateral flow assay. 10 $\mu\text{g/mL}$ BSA in 1X PBS was used as a negative control. The tests ran for 15 minutes and were then imaged.

As shown in Figure 2.6A-D, all four VCP solutions resulted in visible signal at both the test and control lines. The negative control strips, however, also showed a visible signal at both the test control lines, rendering these tests false positives.

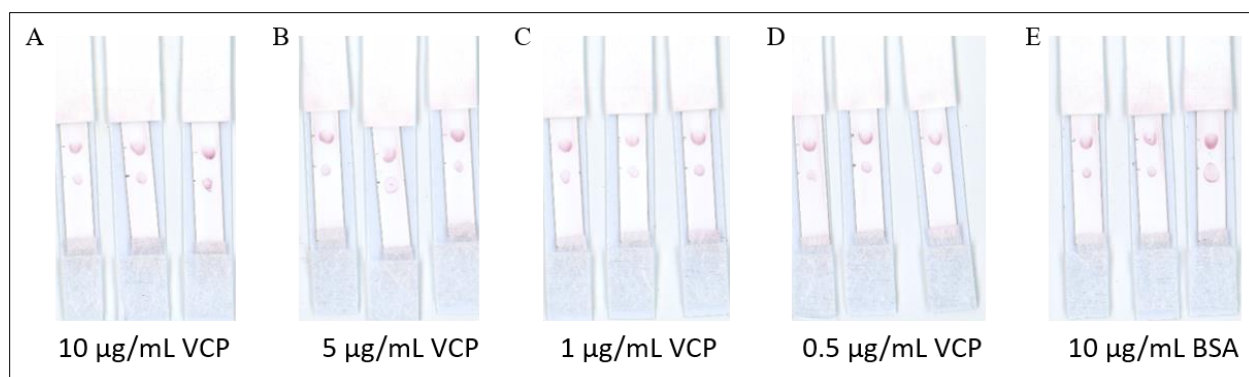


Figure 2.6: Validation of detection of purified VCP on fully integrated lateral flow assays at concentrations of **A.** 10 µg/mL, **B.** 5 µg/mL, **C.** 1 µg/mL, and **D.** 0.5 µg/mL using **E.** 10 µg/mL BSA as a negative control.

The newest fully integrated lateral flow assays were also tested with different amounts of lysed HeLa cells. In the experiments run in Figure 2.7A, 40 µL of HeLa cell lysate containing approximately 1×10^5 , 1×10^4 , 1×10^3 , or 1×10^2 cells was added to each sample pad ($n = 3$ for each cell count). 40 µL of RIPA buffer was used as a negative control.

A qualitative analysis of Figure 2.7, as observed by the unaided eye, shows that test and control spots were visible for all tests that included HeLa cells. For the tests that were run with the RIPA buffer only, the control spots were clearly visible, and the test lines were not. This verified that the conjugated gold nanoparticles were not binding to the M15 antibody dried on the test spot. A quantitative analysis of the test and control spot intensities in Figure 2.7 can be seen in Figure 2.8, which shows that the test line intensities on the negative control strips are smaller than any of the other spots on all the assays, between which there was no significant difference.

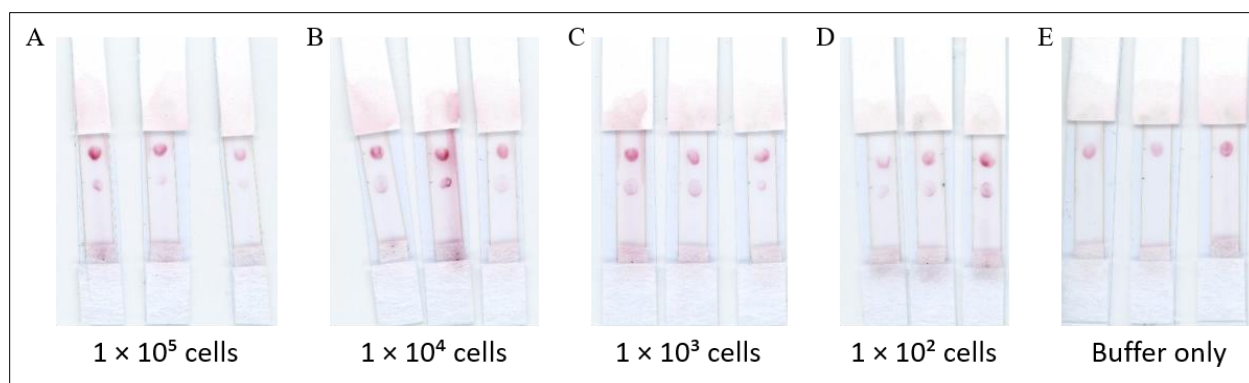


Figure 2.7: Validation of detection of lysed HeLa cells on fully integrated lateral flow assays at cell counts of **A.** 1×10^5 , **B.** 1×10^4 , **C.** 1×10^3 , and **D.** 1×10^2 using **E.** RIPA buffer only as a negative control

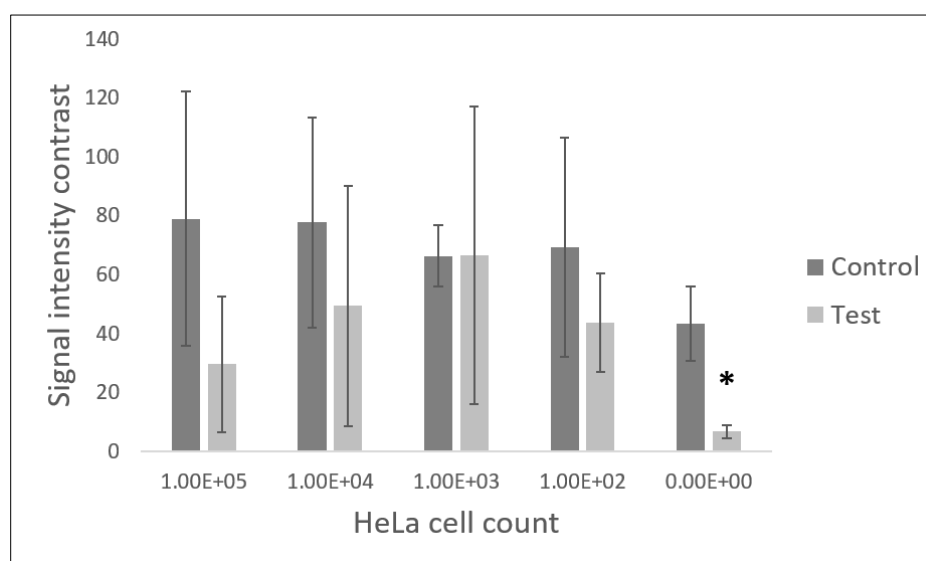


Figure 2.8: Bar chart showing signal intensity contrast of test and control spots on lateral flow assays run with different HeLa cell counts. Error bars represent standard deviation ($n = 3$). The bar with a * (representing the control strips) is significantly smaller than the rest of the bars at $p < 0.20$ using a one-way ANOVA and Tukey's pairwise comparison ($p = 0.174$). *This is not technically statistically significant but that is likely due to the large variation in the signal intensity in the test strips; the control strips' test lines are clearly not visible to the human eye.*

2.4 Discussion

One of the most interesting results in the development of the process for detecting VCP with gold nanoparticles was how dramatically the binding signal was increased by switching from single conjugation to double conjugation, with no other alterations to the assay process. Theoretically, the addition of a second antibody to the conjugation process with no affinity to the

protein of interest should not make a significant difference in the binding signal intensity, since only the primary antibody (in this case, M18) is expected to bind to VCP. It is clearly visible in Figure 2.3, however, that introducing streptavidin-poly-HRP to the conjugation process resulted in a significantly increased binding signal. One possible explanation for this is that the introduction of a second antibody changed the orientation in which M18 attached to the gold nanoparticle, making the outward-facing portion of this antibody more favorable for binding with VCP. Another potential reason for the observed difference is the switch from NHS-activated nanoparticles to plain gold nanoparticles between the single conjugation and double conjugation methods; however, this would be counter-intuitive, as NHS-activated nanoparticles have been associated with better binding outcomes due to the covalent binding between primary amines in the antibody and the ester on the NHS.^{40,41} In this instance, the material switch was made purely in the interest of cost, as NHS-activated nanoparticles are more expensive than plain gold nanoparticles. A variety of publications describe more favorable antibody binding to the desired target with optimal antibody orientation after immobilization on a nanoparticle or surface.⁴¹⁻⁴⁴ Literature in this area uses a variety of chemical techniques for targeting certain features of antibodies to inorganic nanoparticles. Here, however, the biochemistry behind the observed increase in signal in the physical adsorption compared to the amine-specific conjugation is unknown. Further experimentation would be necessary to formulate and test hypotheses regarding this phenomenon. It is also possible to investigate alternative methods for conjugation, as the efficiency of antibody conjugation to nanoparticles and their resulting performance on lateral flow assays has been shown to differ based on conjugation methods.⁴⁵

Based on the clinically relevant amount of protein needed to be detected from a cervical swab, it is possible that additional signal enhancement will need to be implemented. Using gold nanoparticles conjugated to both the VCP detection antibody (M18) and streptavidin-poly-HRP, which permits enzymatic signal enhancement, permits easy incorporation of this additional step into future lateral flow assay iterations if necessary. While current laboratory tests implementing HRP-DAB signal enhancement required the extra step of dissolving DAB and hydrogen peroxide in water before adding the solution to the assay, literature has shown that it is possible to dry both DAB and hydrogen peroxide on a two-dimensional paper network for a self-contained assay that includes signal enhancement.⁴⁶

An important observation in the dot blot analysis of M15 binding to HeLa cell lysate was that there was a visible relationship between binding signal intensity and the number of cells within the lysate. Moving forward into detection of VCP from human cervical swabs, it will be important to know the clinically relevant amount of protein that needs to be detected. This number is currently unknown; however, the potential decrease in signal associated with a decreased number of cells offers an opportunity to back-calculate the amount of protein present by comparing the signal intensity from HeLa cell detection and purified VCP detection. This experiment was attempted with dot blots, but the resulting signals were too unclear to be precisely analyzed and compared (Figure 4.2). There is still potential to successfully perform this experiment in the future, either with another attempt at dot blot comparisons or with a more precise method such as a traditional ELISA.

Regarding lateral flow assay development and optimization, early iterations of the lateral flow assays involved diluting VCP directly in liquid gold nanoparticles and depositing that solution directly onto the sample pad. These experiments produced better binding signal to the test lines than when the gold nanoparticles were dried on the glass fiber pads; however, dried gold nanoparticles are an essential component of these lateral flow assays since liquid gold nanoparticles can only be stored for up to two days before they begin to aggregate and lose their functionality. Early experiments aiming to optimize the drying protocol have produced assays with both improved and worsened binding signal, indicating the dried gold nanoparticles can likely be further optimized to produce a test line binding signal with an intensity comparable to that produced by the liquid gold nanoparticles.

One notable result to consider in this chapter is the false positive lateral flow assays shown in Figure 2.6E. Here, 10 mg/mL BSA produced a binding signal at the test spot that was equal to the test spot of all the VCP lateral flow assays. BSA should not have produced any signal here since the M15 and M18 antibodies should bind to VCP only, and the only molecule that streptavidin would be expected to bind with is biotin. This nonspecific binding must be addressed before the lateral flow assay can be tested with cervical tissue samples; cervical tissues will contain a variety of proteins and it is imperative that the test detect elevated levels of VCP only. One possible explanation for this nonspecific binding is that the concentration of M15 on the test spot, 1 mg/mL, is too high. It is apparent from the lack of a binding signal at the test spot in Figure 2.7E, where the assays were run with buffer only, that the gold nanoparticles themselves are not binding

nonspecifically to the M15 at the test line, ruling out affinity of M18 or streptavidin-poly-HRP to M15 as an explanation for this phenomenon. Further experiments and lateral flow assay optimization must be performed to prevent the detection of any biomolecule apart from VCP at the test spot.

It is important to note that the goal of this point-of-care diagnostic test is to detect an elevated level of VCP, not merely the presence of the protein itself. For this reason, it is essential to determine the precise amount of VCP from a cervical sample that would be indicative of early cervical cancer and to optimize the lateral flow assay conditions to detect that amount accordingly. Therefore, the tests not only need to be redesigned to prevent nonspecific binding, but reagent concentrations need to be adjusted to detect only the clinically relevant concentration of VCP. This will result in a trade-off between specificity and sensitivity; the selected concentration will be selected to reduce Type I and II errors as much as possible, but will err on the side of reducing false negatives since follow-up testing will likely be needed to confirm a diagnosis should patients receive a positive test result.

While the experiments shown in Figure 2.7 detecting HeLa cells on the lateral flow assays showed promising results, given the false positives present when tested with samples containing BSA, additional tests are needed to verify the lack of a false positive result on the negative control tests. First, the tests should be run with the cell growth media, which was removed during centrifugation before the experiments in Figure 2.7. A microcentrifuge was used for these experiments, which could be accessible in some low-resource clinics, but assays requiring as few steps as possible are preferable for all clinics. Furthermore, it is necessary to test a negative control that is a non-cancerous (primary) human cell line to verify that noncancerous human tissue would indeed produce a negative result.

Prior to any clinical testing, once the lateral flow assays have been optimized to sensitively and specifically detect HeLa cells, it will be necessary to test them with human cervical tissue samples. The first step to this process will be determining appropriate tissue preparation methods so the samples can be processed and run on the lateral flow assays. This procedure should be developed without the use of laboratory equipment to facilitate a smooth transition from laboratory testing to eventual clinical testing. Once an appropriate preparation method has been established, the lateral flow assays will need to be optimized to accurately detect known positive and negative tissue samples. Finally, to verify their efficacy, blinded trials with unidentified tissue samples will

be run and then validated through a clinical collaboration pre-established by Dr. Mohammed (Clinical Sciences Translational Institute and Women's Global Health Initiative seed grant).

Throughout and following the robust optimization and validation of accurate cervical cancer detection from tissue samples on the lateral flow assays, user-centered design will be implemented to ensure that the entire process of sample collection, preparation, and detection will be compatible with the cultural and infrastructural parameters of the environment in which the assays will eventually be used. Two routes of clinical and public health collaborations will be employed for usability verification. A collaboration with Dr. Natalia Rodriguez, a professor in the Department of Public Health at Purdue University, has been formed to begin outreach to community health workers in underserved communities local to Indiana and the United States. Steps that can be taken immediately to ensure user-centered design include interviewing these health workers and other researchers and clinicians with healthcare experience in low-resource areas to assess what technical aspects are necessary for the eventual implementation of this device. Such specifications can then be included throughout device iterations. Additionally, as mentioned previously, Dr. Mohammed has established collaborations with clinicians in Zambia who are prepared to test the devices once they reach an appropriate stage in the development process. Locally, collaborations can be established with outpatient clinics in both low and high-resource areas of the United States to both test the device's accuracy in a clinical setting and receive feedback regarding the use of the from community healthcare workers to nurses and doctors. Feedback from all sources will be paramount in designing a device that can accurately identify early cervical cancer using methods that are culturally and infrastructurally compatible with the communities in which they will be used.

The ultimate vision for these lateral flow assays is for their use as a tool to efficiently allocate limited resources for cancer diagnosis and treatment in low resource areas to the patients who need it most. The test will serve as a broad screening measure that allows a greater population of patients to be tested than is currently possible with present models for outpatient clinics. Local clinics can work with community healthcare workers to distribute the test within local communities. Patients should be able to take the test and have the results given and explained to them within their own homes. This will require optimized sample collection methods, but recent developments in self-testing vaginal swabs for STI testing show promise for a similar method to be developed for self-testing cervical swabs. Additionally, appropriate training for community healthcare

workers must be developed within the cultural parameters of their communities so they can effectively communicate the need for testing to patients.⁴⁷ When patients who are highly likely to have early stage cancer are identified, community health workers can help them with access to a local clinic for follow-up testing, which could include some of the currently existing methods like VIA/VILI, or traditional cytological screening methods like the Pap smear based on available resources. Close collaborations with clinicians and community workers can ensure that at-risk patients are not lost to follow-up and that testing, treatment, and follow-up screenings are administered as appropriate. Using this methodology, limited testing and treatment resources can be saved for patients who are the most at risk, and has the potential to better identify and connect those patients by reaching a larger population with simple and widespread screening provided by the detection device described in this chapter or an alternate method that works in a similar fashion.

3. FLUIDIC CHARACTERIZATION OF LATERAL FLOW ASSAYS FOR EFFICIENT MULTI-STEP BIOMARKER DETECTION

3.1 Literature Review

As discussed in Chapter 1, there is great potential for lateral flow assays to be significantly improved through designs that increase specificity and sensitivity and permit the incorporation of more complex reactions. Re-engineering LFAs with sample flow delays and redirections has improved their sensitivity, specificity, and breadth of analyte targets by optimizing reactions. For example, geometrically-tunable absorbent pad shunts⁴⁸ and stacked films with different reagents⁴⁹ can delay fluid for sequential reagent delivery, and printed wax barriers in the paper membrane slow fluid flow to permit longer reaction times.⁵⁰ These methods, however, while simple and hands-free, are only able to delay fluid flow for a limited amount of time, making prolonged incubations within the device infeasible. Conversely, timed delivery of multiple reagents for signal amplification can be achieved through reusable rotational valves to manually connect multiple assay stages⁵¹ or two-dimensional paper networks using multiple inlets of different lengths and disconnecting portions.⁵² While these methods provide more control over extended delay time and precise reagent delivery, their requirement for manual operation limits their user-friendliness. Previously, thermally-actuated wax valves were demonstrated to offer complete, timed control of fluid obstruction and release in an LFA, permitting multiple reactions within a single device.⁵³ The integrity of the valves, however, is susceptible to surfactants present in the reactions and must be optimized for assay conditions.

Developing and optimizing any LFA, especially with more complex components as described above, is a complicated and highly iterative process comprising many trial-and-error experiments to identify the best conditions for each sample and assay type.⁵⁴ Biological LFA components have a wide range of variable characteristics, so analytical techniques that assess their properties can inform design parameters.⁵⁴ Such techniques include surface plasmon resonance and bioluminescence imaging, which determine the rate kinetics of binding reactions and inform optimal target-probe pairs.⁵⁵ However, material heterogeneity and mass transport limitations prevent these techniques from being relevant to binding kinetics within LFAs.⁵⁶ To overcome these practical limitations, mathematical modeling techniques can minimize costly experimentation by

using fundamental transport principles to inform LFA design. One such recent model simulates analyte dynamics by defining dimensionless numbers describing relative flow rate and analyte concentration.⁵⁷ Other models validate mathematical predictions with experimental data. For example, Liang and colleagues experimentally investigated pre-mixed and sequentially-added reagents on an LFA for malaria detection, using those results to validate a COMSOL model to explain how different binding kinetics yielded different results.⁵⁸ Notably, Gasperino and colleagues combined mathematical descriptions of fluid behavior in porous membranes, including the Lucas-Washburn Equation, Darcy's Law, and the Richards Equation, to model the detection of a malaria antigen in an LFA. This model was validated against real LFAs with different antigen concentrations and used to develop a software basing LFA design decisions on fifteen reaction scheme hypothesis.⁷

While mathematical models can accelerate the LFA design process, accurate measurements are required to inform their parameters. The models described previously are limited by their exclusive treatment of bulk behavior and neglect of experimental data analyzing sample flow through the porous membrane at the particle level. A better understanding of nanoparticle transport within LFAs would improve existing models⁷ and validate our assumptions of membrane homogeneity, laminar flow and binding kinetics. One possible solution lies in the availability of micro-particle image velocimetry (μ PIV) as an empirical evaluation method for particles traveling through an LFA. This method was employed in 1998 to measure velocity fields of fluorescent particles in a 30 μ m cylinder.⁵⁹ More recently, with the growing field of microfluidic biomedical devices, the need for more advanced flow analysis resulted in expanded applications, such as fluorescent imaging to minimize light scattering from channel walls and the identification of the impact of particle zeta potential⁶⁰. Furthermore, μ PIV has been used in more complex environments, resulting in work providing parameters for modeling solute transport in porous media by identifying predictive pore network models and particle tracking methods to overcome common errors,⁶¹ and methods for measuring three-dimensional particle motion in pore-based models.⁶² These more complex analyses have expanded existing particle transport models, identifying phenomena such as maximum particle velocities at the center of pores⁶² and local pore-scale variations due to membrane tortuosity, which can be three-dimensionally visualized over a broad range of length scales using confocal microscopy.⁶³ μ PIV has also been used to quantify

pore-scale velocity in low Reynold's number flow⁶⁴ and particle velocity through signal and dual-depth silicon-based pore masks to demonstrate flow behavior at pore size transition zones.⁶⁵ μ PIV could provide unique insight into the microscopic behavior of fluid flow in LFAs to validate fluid delay mechanisms and elucidate in-flow binding properties.

Here, we optimize thermally actuated wax valves for precise fluid delay and delivery and validate those principles with robust experimental and computational analyses. We identify optimal valve geometry and the resulting fluid behavior and explain the entire process with mathematical models. Furthermore, we develop a novel method for imaging and evaluating microscopic particle flow in LFAs using μ PIV, validating underlying assumptions with scanning electron microscopy and explaining the observed relationship between macroscopic and microscopic flow. Finally, we discuss how this analytical and mathematical data can be combined and synthesized to inform more intelligent and efficient LFA development.

3.2 Methods

3.2.1 Nitrocellulose properties and test strip construction

Test strips were constructed by adhering a SelfSeal laminating sheet (3M) to one face of AE99 unbacked nitrocellulose membrane (GE Healthcare). The laminated nitrocellulose was cut by hand with a razor blade into 3.5 cm x 0.5 cm strips.

3.2.2 Scanning electron microscopy (SEM)

To verify membrane surface and cross-sectional homogeneity, a scanning electron microscope (FEI NOVA nanoSEM Field Emission) was used to image the membrane surface and edge at 1000X, 1500X, and 5000X. Images were also taken using cryo-SEM of the 40 nm green fluorescent nanoparticles (ThermoFisher) used for video analysis, both independently and within the nitrocellulose membrane to elucidate the relationship between nanoparticle and membrane pore size.

3.2.3 Macroscopic imaging

Test strips were constructed as described in Section 1.2.1 and placed laminate side down on a piece of double-sided tape next to a ruler with 0.5 mm increments. A 0.5 cm x 1 cm glass fiber pad was placed at one end of the test strip. To evaluate flow behavior, 40 μ L deionized (DI) water was added to the glass fiber pad and subsequently flowed into the nitrocellulose membrane. A Samsung S7 phone was placed on top of a 15 cm container and used to record video from the time water was added to the sample pad until it reached the end of the nitrocellulose strip.

3.2.4 Macroscopic analysis

Videos were processed into a sequence of images with one image for each second of video. These images were loaded into ImageJ, processed to enhance contrast between the water and the paper, and fit with a five-section grid dividing the membrane into equal areas at the middle and edges of its surface. The location of the fluid front, measured with respect to a ruler adjacent to each test strip, was recorded for each section. To compare observed data to our theoretical prediction, a Lucas-Washburn curve was fit to this data in MATLAB, and the derivative of this curve was calculated at different points of interest to extract the instantaneous macroscopic fluid velocity.

3.2.5 Wax valve analysis

Wax valves were designed to have straight, concave, and convex geometries, as shown in Figure 3.1. Valves of different geometries were compared across equal printed surface areas to ensure wax volume as a controlled variable. All valves were designed in Adobe Illustrator: straight valves consisted of a simple rectangle; concave valves were designed by subtracting ellipses from the top and bottom of a rectangle to render the total ink area equal to that of the straight valve; convex valves consisted of an ellipse with an area equal to that of the straight valve. Valves were printed with solid-wax ink onto AE99 nitrocellulose membrane using a Xerox ColorQube 8570. After printing, the printed membranes were heated for 60 seconds at 80°C in a tabletop oven (VWR) to permit penetration of the ink through the depth of the membrane, closing the valve. Once the valves were closed, the nitrocellulose was cut by hand into 5 mm strips with one complete valve on each strip.

To analyze flow past opening valves in real time, prepared strips with fully closed valves were placed on a 164.3Ω polyamide thin film heater (Cole-Parmer) and sealed with a laminating sheet to limit fluid evaporation from wetted strips, as shown in Figure 3.1B. 40 μL of water was manually deposited onto one end of the strip, then, the entire strip was heated by applying 2.1 A of current to the heater to melt the wax, opening the valves and permitting fluid passage. Macroscopic flow behavior was evaluated by first characterizing the amount of time for fluid to travel through the valves and then calculating its flow rate through the nitrocellulose past the valve ($n = 3$ for both evaluations).

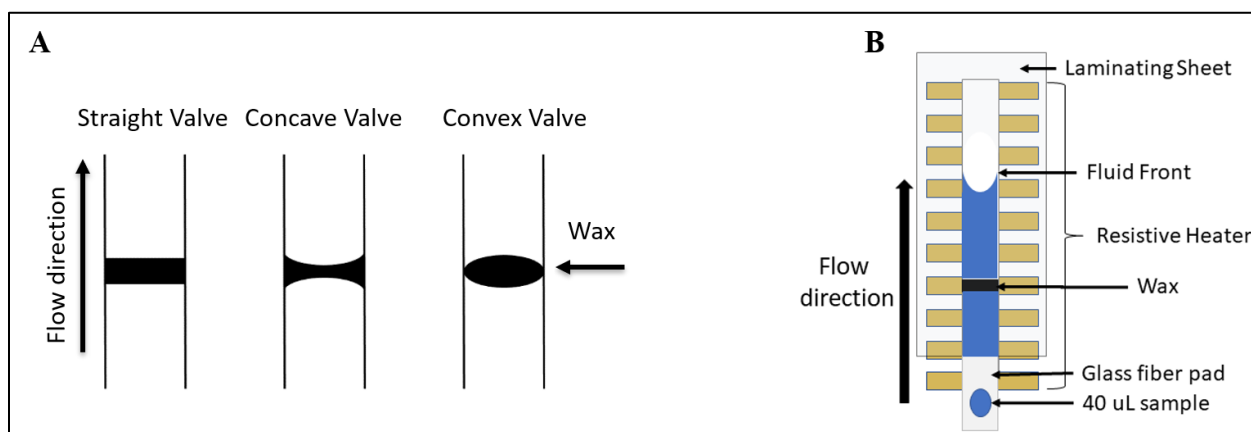


Figure 3.1: **A.** Different valve geometries. **B.** Experimental setup for macroscopic flow analysis.

3.2.6 Microscopic imaging

To visualize the microscopic properties of fluid flow within the test strips, fluorescent nanoparticles were imaged as they traveled through the nitrocellulose membrane. To assemble the test strips for microscopic imaging, double-sided tape (3M) was adhered to a glass microscope slide, as shown in Figure 3.2, overhanging the slide by 1 mm on one end and 14 mm on the other end. A 0.5 cm x 1 cm glass fiber pad (Millipore) was adhered to the 1 mm overhang of the laminating sheet. Next, the paper test strip was placed paper side down with one end overlapping the glass fiber pad by 1mm and the remaining portion of the strip adhered firmly to the laminate sheet.

To image particle motion within the paper test strip, as shown in Figure 3.2, the glass slide assembly was placed paper side down on the stage of an inverted fluorescent microscope (Zeiss) and illuminated with an AlexaFluor 488 light. A 40X magnification was used to focus on the

membrane surface at a region of interest in a 116.22 by 116.22 μm field of view. 40 μL of 0.02% w/v green fluorescent nanoparticles were added to the glass fiber sample pad, after which they flowed into the nitrocellulose membrane. When the nanoparticles became visible in the selected field of view, a ten second video was captured at 40 frames per second with 2-by-2-pixel binning. To analyze discrepancies in particle velocity along the length of the test strip, videos were taken 5, 10, 15, 20, and 25 mm from the sample pad end of the membrane ($n = 3$ videos for each field of view).

3.2.7 Microscopic analysis

Micro-particle image velocimetry (μPIV) was used to assess the particle velocity from the microscope videos of fluid flow within the nitrocellulose membranes. Microscope videos were processed from the microscope software format (.czi) to a sequence of bitmap (.bmp) images, with one image per video frame, using a MATLAB code developed by Hui Ma. The μPIV software EDPIV was used to convert the sequence of .bmp images into a .lis file, which was then uploaded into EDPIV as an image group.

Prior to processing, an Overlapping- boundary mask was created over the sequence of images to subtract areas of obstructed flow from the evaluation. After this boundary mask was applied, an EDPIV evaluation was run with a 128 by 128-pixel window size, a 64 by 64-pixel grid size, a 63-pixel searching radius, central difference interrogation, central window shifting, and 4-pixel image correction. The resulting vector field was evaluated as an average function of the entire image set, and each evaluation was run in three iterations. After the first evaluation, the resulting velocity data was interpolated onto a 32 by 32-pixel grid, and the evaluation was run again with the same parameters in three iterations. These settings were used for evaluating each video. The vector fields from the EDPIV analyses were saved as .dat files for analysis and processing in MATLAB.

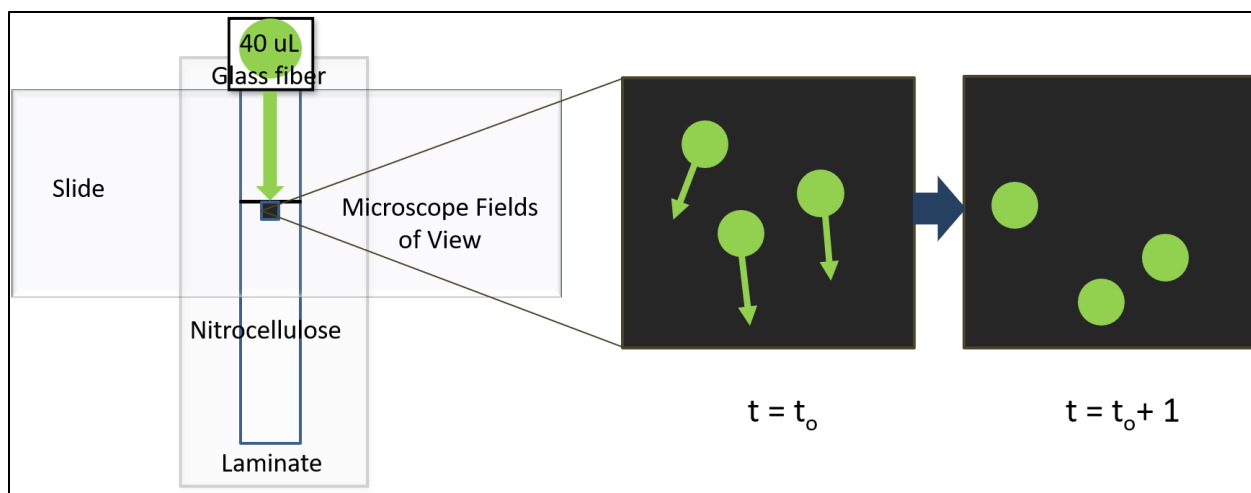


Figure 3.2: Diagram of microscope setup for imaging particle flow in nitrocellulose membrane

3.3 Results

3.3.1 Membrane homogeneity validation

The structural properties of the nitrocellulose membrane used in these LFAs were analyzed to substantiate the underlying assumptions in our models. Scanning electron microscopy (SEM) revealed surface (Figure 3.1A) and cross-sectional (Figure 3.1B) homogeneity. Our quantitative fluid analysis used the Lucas-Washburn and Richards equations; these images helped us justify the degree to which our models were valid under the assumptions associated with those equations. Additionally, SEM images of the fluorescent nanoparticles used for μ PIV flow analysis revealed their shape and size (Figure 3.1D) compared to the shape and size of the membrane's pores (Figure 3.1E), further informing the assumptions and evaluations of our fluid flow analysis. Finally, wax melted into the nitrocellulose membrane was imaged on both the surface (Figure 3.1F) and cross section (3.1C) of the membrane, demonstrating how the wax obstructs the open pore structure within the membrane.

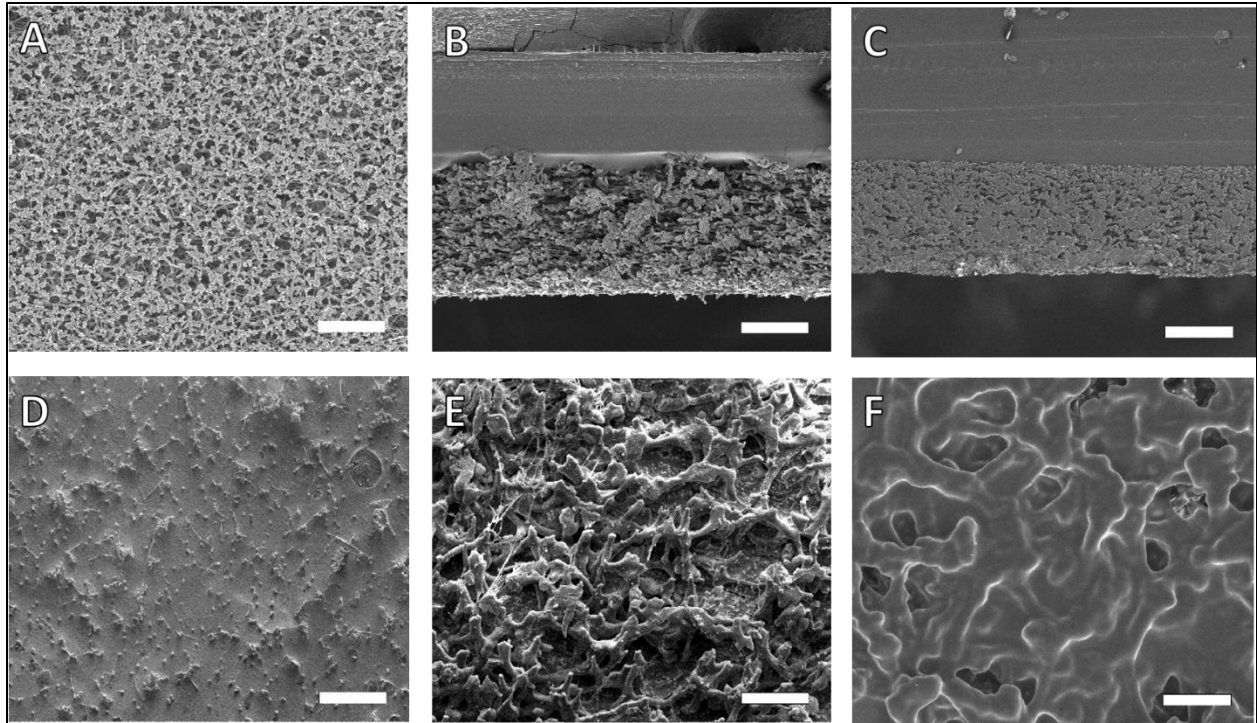


Figure 3.3: **A.** SEM image of surface of nitrocellulose membrane (1000X magnification). **B.** SEM image of cross-section of nitrocellulose membrane demonstrating homogeneity of pore structure throughout membrane depth (100X magnification). **C.** SEM image of cross-section of nitrocellulose membrane with wax melted throughout (1000X magnification). *Image courtesy of Elizabeth Phillips* **D.** Cryo-SEM of 400 nm green fluorescent nanoparticles (5000X magnification). **E.** Cryo-SEM of 400 nm green fluorescent nanoparticles in nitrocellulose membrane (5000X magnification). **F.** SEM of nitrocellulose membrane with wax melted throughout (5000X magnification). *Image courtesy of Elizabeth Phillips. Note: the white scale bar in the bottom right corner of each image represents 50 μm in Figures 3.3 A-C and 10 μm in Figures 3.3 D-F.*

3.3.2 Macroscopic flow analysis

Having confirmed that particles would flow freely through the membrane and liquid would be obstructed by wax valves, we then evaluated macroscopic fluid flow in order to determine how valve geometry influences the rate and pattern of fluid traveling through a multi-stage lateral flow assay with wax valving. Indeed, macroscopic analysis of fluid flow through valves showed that both valve actuation time and the rate of fluid flow past actuated valves were significantly affected by valve surface area and geometry.

Actuation time is defined as the amount of time between when the resistive heater is turned on and when fluid first begins to flow through the valve. Figure 3.3A shows the difference in

actuation time between straight, concave, and convex valves of equal surface area (5 mm²). Here, concave valves result in the shortest average actuation time when compared to straight and convex valves of the same surface area. Previous work has demonstrated that in straight valves, fluid is observed to flow through the edges of the valve first.⁵³ Therefore, it follows that concave valves, which are thinner at the edges of the test strip than straight or convex valves, would actuate faster than those valves with the same total surface area but a larger width of wax at the edges.

In addition to actuation time, macroscopic experimental analyses investigated the effects of different valve shapes and sizes on fluid flow rate past the valve. Figure 3.3B compares the distance traveled by fluid past straight, concave, and convex 5mm² valves. With all valves, fluid traveled slower than it would through unobstructed nitrocellulose, but concave valves clearly resulted in the fastest fluid flow of all the valves, straight valves resulted in slower fluid flow, and convex valves resulted in the slowest fluid flow. This pattern was consistent across all three valve sizes investigated (Appendix B, Figure 4.2).

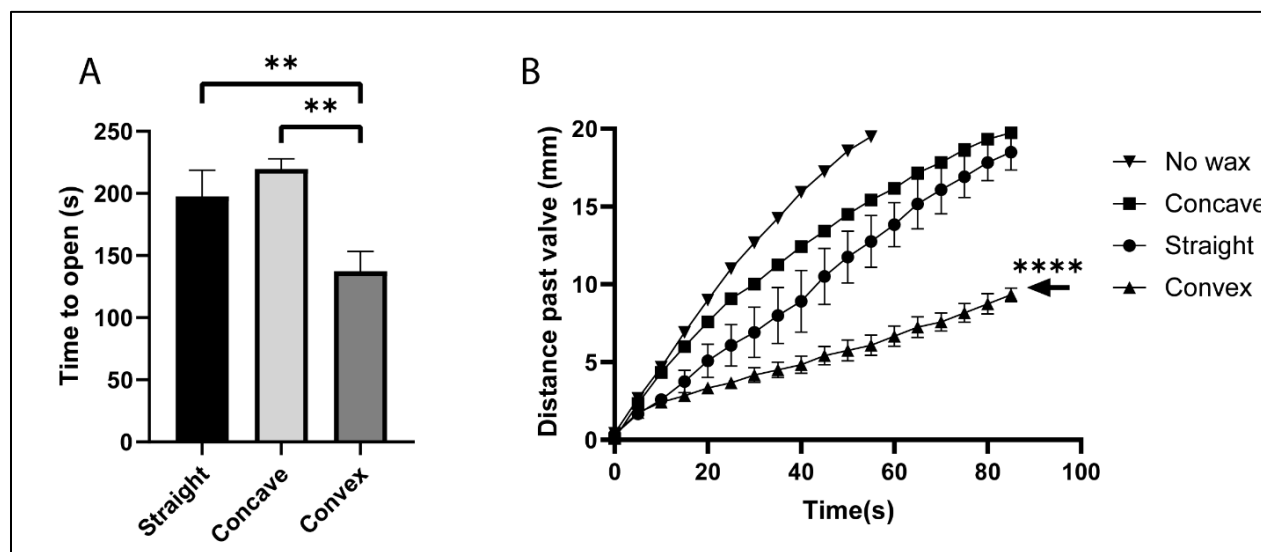


Figure 3.4: **A.** Actuation time of medium valves (surface area = 5 mm²) of different geometries (n = 3 and error bars represent standard deviation). **B.** Rate of fluid flow past medium valves of different geometries compared to flow in unobstructed nitrocellulose (n = 3 and error bars represent standard error of mean).

3.3.3 Macroscopic flow modeling

In many preliminary experiments investigating macroscopic fluid flow, the shape of the fluid front was observed to vary greatly across the width of the test strip. For example, the fluid at

the edges of the strip would advance faster than the fluid in the middle of the test strip. This pattern, observed with fluid traveling through unobstructed nitrocellulose and sometimes with fluid traveling past a valve, contradicts the expectations of traditional laminar pipe flow which follows a parabolic profile fastest in the middle of the test strip.⁶⁶ For this reason, we developed a MATLAB model to further characterize macroscopic fluid flow in the nitrocellulose membrane and the effect of valve geometry on fluid front shape, and to compare our theoretical characterization to experimental observations.

Figure 3.4 shows the experimental variation in flow rate across the width of the test strip following different valve geometries of equal surface area. With straight valves (Figure 3.4A), there was no statistically significant difference in the distance traveled by the fluid front across the width of the test strip, but an extremely large amount of variation was present between the trials, likely due to different and uneven fluid fronts in each individual trial. Concave valves (Figure 3.4B) resulted in both the most even fluid front and the smallest standard error in fluid front distance at each time point. Finally, within the first minute of flow past convex valves (Figure 3.4C), a largely uneven flow front was observed; further time data (not shown), however, shows converging flow rates as the front fully develops with more time (after 90 seconds).

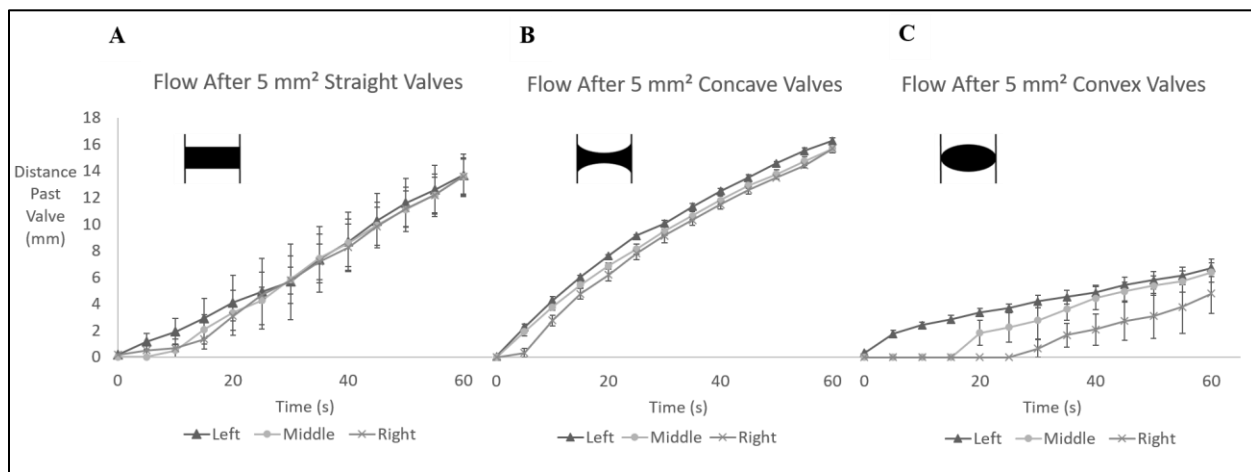


Figure 3.5: Macroscopic fluid velocity in the left, middle, and right of the nitrocellulose membrane past **A.** straight, **B.** concave, and **C.** convex valves. Error bars represent standard error of the mean ($n = 3$).

To create a mathematical model describing the observed differences in fluid front flow rates and patterns, the Richards equation was applied to the porous membrane system to describe partially saturated flow:

$$\frac{\partial \theta}{\partial t} = \frac{\partial}{\partial x} \left(D(\theta) \frac{\partial \theta}{\partial x} \right) + \frac{\partial}{\partial y} \left(D(\theta) \frac{\partial \theta}{\partial y} \right),$$

where θ is the volumetric content of liquid in the membrane, $D(\theta)$ is the equivalent diffusivity, and x and y are two dimensions of the nitrocellulose membrane. Here, the nitrocellulose membrane was assumed to be a two-dimensional system with four edges, and the effects of gravity were neglected. One edge was assumed to be in contact with a water reservoir; here, a Dirichlet boundary condition was applied.⁶⁷ On the other three edges, a Neumann boundary condition with no flux was applied.⁶⁸

In addition to these boundary conditions, this model assumed that air inside the nitrocellulose could only travel through the thin membrane layer and escape from the edges, since it was sealed on the top surface, changing the effective porosity of the nitrocellulose and thus the gas permeability of the medium.⁶⁹ Gas transport in a porous medium can be described by an equation similar to Darcy's law:⁷⁰

$$J = -\frac{K}{kT} \nabla p ,$$

where K is gas permeability and ∇p is the pressure gradient. This equation differs from Darcy's law in that T , temperature, replaces liquid viscosity. Furthermore, since the Lucas-Washburn equation can be derived from Darcy's law,⁷ the velocity of gas in a porous medium can likewise be described with a relationship similar to the Lucas-Washburn equation:

$$L = C\sqrt{t},$$

where C is a constant based on material, gas, and temperature properties of the system. Since the nitrocellulose membrane is sealed on the top and bottom surfaces, the velocity of air traveling through it was parallel to the direction of the pressure gradient at each point on the liquid fluid front. The air in the center of the membrane took a much longer time to escape from the membrane than air closer to the edges, decreasing the permeability of the membrane to liquid traveling through it. Therefore, the diffusivity factor $D(\theta)$ from the Richard's equation was modified to include a function, $f(x)$, with a high boundary value and a steep decrease in value approaching the center of the membrane. $F(x)$ is an exponential function fit to the experimental data for the purpose of this model.

$$D'(\theta) = D(\theta) + f(x)$$

This value was substituted into Richard's equation and solved to produce flow rate patterns for wax-free systems shown in Figure 3.5.

In systems that included wax valves, the presence of wax changed both the porosity and permeability of the nitrocellulose membrane. When wax is heated, the phase changes gradually, and it flow through the membrane like a viscous liquid, as can be described by the Lucas-Washburn equation. Due to the boundary effect of heat conduction, different wax valve geometries resulted in a different melting ratio at each point of the valve. Experimental observations suggested that the wax may only need to melt partially to permit fluid flow in certain regions such as the edge of the membrane or the narrow region in the center of the concave valve. Considering these observations, the diffusivity was modified for each geometry with respect to the measured data:

$$D_i = D'(\theta) + F_i(x),$$

where $F_i(x)$ is dependent on the change of permeability in the wax valve regions and the geometry of the wax valves, with different properties for each i valve. These diffusivity equations were substituted into the Richards equation and solved to produce the results for fluid flow velocity past each different valve, as shown in Figure 3.5B and C.

From these mathematical models, Figure 3.5A shows the flow rate for fluid through the unobstructed nitrocellulose at the edges, where the fluid progresses at a faster rate, and at the center, where it travels more slowly. Figure 3.5B shows the fluid front profile at equally spaced time points for fluid flowing through unobstructed nitrocellulose and past straight, convex and concave valves. This figure's visualization of fluid front patterns agrees with experimental observations, where a parabolic profile is observed with fluid progressing faster along the edges of the paper. Finally, Figure 3.5C compares the overall flow rates of fluid traveling past each valve to that of fluid traveling through unobstructed nitrocellulose, again agreeing with experimental data showing fluid traveling fastest through unobstructed nitrocellulose, followed by fluid traveling past concave valves, then straight valves, and finally traveling the slowest past convex valves.

Mathematical modeling theory and results courtesy of Hui Ma.

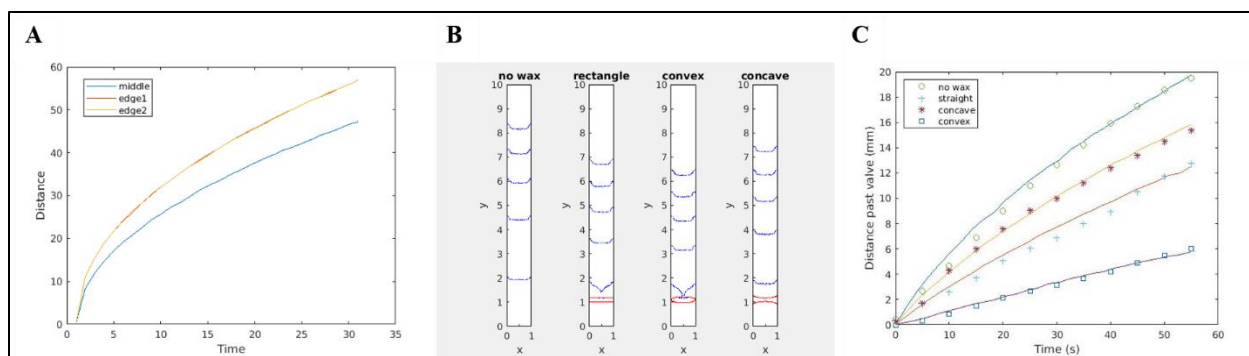


Figure 3.6: Mathematical model describing flow in nitrocellulose membranes. **A.** The macroscopic flow rate unobstructed by wax valves (unitless distance and time). **B.** Flow pattern along nitrocellulose membrane at equally spaced time points past valves of different geometries. **C.** Flow rates past different valve geometries. *Images produced by Hui Ma.*

3.3.4 Microscopic flow analysis

Following analysis of the macroscopic properties of fluid flow through nitrocellulose membranes, microfluidic properties were investigated to compare transport patterns at the particle level to those observed at the bulk flow scale. Since relevant events in lateral flow assays such as nanoparticle binding occur at the micro and nanoscale, these experiments aimed to investigate how particles travel through the membrane's pores to elucidate how lateral flow assays can be better designed with microscale transport considerations.

To visualize and quantify microscopic flow properties within the nitrocellulose membrane, 400 nm fluorescent nanoparticles were imaged at different locations along the middle of the membrane test strips and quantified with μ PIV using the EDPIV software. For the purposes of this analysis, the middle of the membrane was observed for the sake of consistency in comparing videos as the SEM membrane images showed more aberrations in membrane homogeneity near the membrane edges. 10 second videos were taken in triplicate at 5, 10, 15, 20, and 25 mm from the sample loading location, beginning when particles first entered the field of view. These videos were then processed in EDPIV to reveal vector fields describing particle motion through different fields of view, as shown in Figure 3.7 for a video taken 15 mm from the sample end of the membrane. These vector fields were plotted over a composite image of all particles throughout the video to demonstrate their alignment with observed flow patterns. Histograms of these vector fields were also created to visualize the distribution in velocity vector lengths within the field.

Vector fields and histograms representative of videos taken 5, 10, 20, and 25 mm down the membrane can be seen in Figure 4.3 in Appendix B.

As shown in Figure 3.7, the distribution and length of velocity vectors agrees relatively well with the flow of particles throughout the video, demonstrating that particle motion can be accurately measured and quantified using these methods. The histogram of vector velocities shows that velocities are skewed right, with many very small velocities (0 to 4 mm/s and trailing off toward 12 mm/s). This is likely due to areas of the membrane (the dark areas in Figure 3.7) in which either particle flow or visualization of particle flow is obstructed. This pattern of right-skewed histograms was observed at various levels for every video taken based on differing degrees of obstruction in each different field of view.

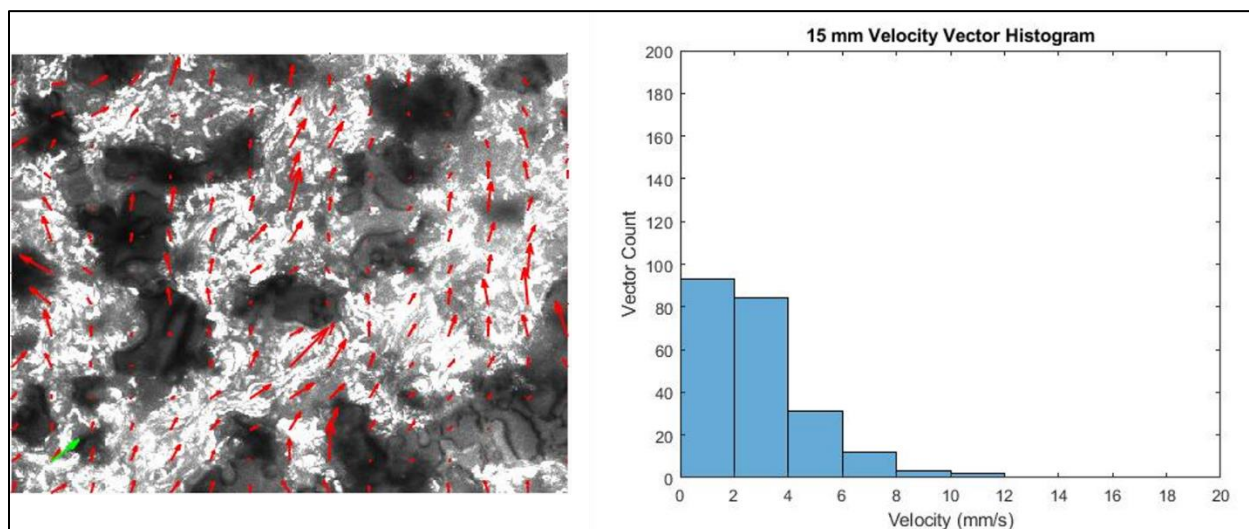


Figure 3.7: **Left:** All 400 images from a 10 second time series taken 15 mm from the sample pad in the center of the membrane combined into a single image to display locations of visible particles, with an overlaying vector field from EDPIV analysis (red arrows; green arrow represents the length of a 1 mm/s velocity vector in both the x and y directions). **Right:** Histogram reflecting the velocity distribution of all 225 vectors in this analysis.

3.4 Discussion

The Lucas-Washburn equation assumes the porous material consists of straight, parallel cylinders with no pore interconnection and a constant cylinder diameter, and thus does not take tortuosity into account.⁷¹ Clearly, this is very oversimplified in the case of the nitrocellulose membrane, but the SEM images show both surface and cross-sectional consistency in pore size;

thus, we conclude flow through this material can reasonably be roughly estimated with the Lucas-Washburn equation. Conversely, the Richards equation is based only on properties of the material itself and does not make any assumptions about the shape or size of the pores, considering only average properties.⁷¹ From the SEM images, it is reasonable to conclude that the average material properties are representative of each individual location on the membrane, so the Richards equation is also a reasonable model of fluid flow in the nitrocellulose membranes.

A key takeaway from the cryo-SEM images is the size of the particles in relation to the size of the membrane pores. In Figure 3.3E, it is apparent that the 400 nm particles are significantly smaller than the cavities within the nitrocellulose membrane through which they flow. Of course, this does not mean that the particles cannot become trapped in areas where pores are obstructed or when the material fiber forms cavities that are too small for the particles to pass through. Indeed, some particles were frequently observed to become stuck during experimentation, especially in less homogenous areas of the membrane, such as the edges. Nevertheless, for the purposes of this analysis, the size relation between the particles and the membrane pores was sufficient to assume that the particles aligned with the bulk transport patterns of the fluid reasonably well.

An interesting result of the macroscopic analysis was the counterintuitive relationship between actuation time and flow rate within the convex valves. These valves had the fastest actuation time and yet the slowest flow rate following actuation. Conversely, concave valves took the longest to actuate but resulted in the fastest flow rate. The main difference between actuation of these two different valves was the location across the strip where flow was first observed. With convex valves, flow was always first observed at the edges of the membrane, similar to straight valves. In contrast, concave valves most often resulted in fluid flow through the middle of the valve first. Due to these divergent behaviors, concave valves quickly resulted in a continuous fluid front as soon as the flow reached both edges of the paper, while flow after convex and straight valves took longer to fully develop into a continuous fluid front. Thus, the location where fluid first travels through the valve affects the overall flow rate of that fluid downstream.

Another notable aspect of the macroscopic data was the large amount of variation present in the flow rate of fluid past the straight valves compared to the concave and convex valves. A possible explanation for this is an uneven conductivity of heat across the valve given the greater wax-air interface at the edges of the membrane and the downstream edge of the valve as compared to the wax-liquid interface at the upstream edge of the valve. Since the straight valve was the same

width across the entire strip, the valve may have opened more or less in different locations depending on the heat distribution; in Figure 3.5, for example, flow past all valves consistently occurred later through the right side of the valve than it did through the left. Because the valves are symmetrical, this could only be due to a difference in heat distribution. Since the actuation time and flow rate data suggests that the location that fluid passes through a valve directly affects its flow rate, it follows that straight valves, which may actuate in different locations, exhibit great variation in flow rate. Future work could use computational modeling or a highly sensitive infrared camera to investigate possible differences in heat distribution across the resistor.

While the mathematical model of macroscopic fluid flow is a valuable tool for visualizing expected patterns and explaining them based on known phenomena of transport within porous media, additional investigations are needed to refine the model. Ideally, future models will be based entirely on measured properties and theoretical flow properties instead of fitting some of the data to experimental results. Specifically, the diffusivity in the Richards equation should be measured and included in the model instead of fitting that value to an exponential function defined by experimental results. Despite these limitations, this mathematical model is still an interesting way to see how counterintuitive flow results, such as the deviance in flow rate and actuation time observed with different valve geometries, can be described mathematically. The model used here will serve as an effective base for future, more refined models that more accurately account for different parameters defined by existing fluid equations in literature.

Understanding the ways that flow rate can be controlled by altering valve geometry is essential for intelligent multi-step assay development. This data facilitates troubleshooting of common issues with lateral flow assays, specifically more complex ones that require sustained incubation times and multiple steps as facilitated by the valves investigated here. For example, a multi-step lateral flow assay with high amounts of undesired background signal can be remedied by a faster sample flow rate induced by a concave valve. Likewise, an assay with low signal intensity can be improved by decreasing the flow rate of the sample across the signal line using a convex valve.

In addition to flow rate, understanding how to manipulate the shape of the fluid front is especially helpful in multi-step assays. For example, in a two-dimensional paper network, fluid that travels faster to one inlet than it does to another could be problematic for assay efficacy. Or, a sample that interacts with one side of dried capture reagents on a test line before it interacts with

the other could be problematic in obtaining the correct signal. On the other hand, an uneven fluid front could also be exploited for more effective multi-step assays. In one such instance, it might be helpful for a sample to separately reach opposite side outlets of a two-dimensional paper network before it travels down the main strip, drastically showing the main inlet fluid flow. With the push for the development of more complex yet self-contained assays, an empirical understanding of ways to manipulate fluid flow simply and effectively will be invaluable for efficient device design.

The microscopic analysis of particle flow within the membrane and resulting quantitative description with PIV-generated vectors is an entirely novel development in the realm of investigating paper-fluidic transport properties. The results in this chapter describe an effective investigation method and serve as a proof-of-concept for this form of analysis. This particle-scale velocity analysis within a porous membrane promises to serve as a valuable tool in more precise analyses of the biophysical phenomena driving paper-based diagnostics.

A few major limitations prevented robust quantitative analysis of the microscale particle velocities described here. Most notably, as shown in the histograms in Figure 4.3 (Appendix B), there was a wide distribution of calculated velocities in each video, and that distribution varied greatly between videos. At the scale of the field of view permitted by the microscope, there was a large amount of local variation in membrane structure. For this reason, it was not possible to discern statistically significant differences in flow patterns and velocities between videos taken in triplicate at the same location across different membranes. There are a few possible ways in which future work can remedy this limitation. First, better test strip fabrication methods could be employed to limit user error. Specifically, here, laminate was manually applied to unbacked nitrocellulose due to particle visualization limitations through pre-backed nitrocellulose. While effective at the macroscale level, at the microscale level, it is likely that this resulted in local membrane deformities such as small bubbles of air and uneven crushing of the membrane. Each of these could be plausible explanations for the areas of flow or visualization obstruction observed in each video. Fewer or more consistent obstructions to flow would likely result in a narrower velocity distribution and permit robust mathematical analysis of the velocity vectors. Ideally, this could result in comparing instantaneous velocities at each location to the instantaneous velocity derived from fitting macroscopic data to relevant fluid flow models to understand how

macroscopic flow compares to particle-scale flow within porous membranes, a relationship that is absent from literature with experimental justification.

In addition to resolving aberrant membrane properties, an improved analysis of particle flow would include treatment of different particles, specifically with properties more relevant to those used in paper-based assays. As one example, 40 nm gold nanoparticles are commonly used in basic colorimetric lateral flow assays such as the home pregnancy test. These particles are ten-fold smaller than the 400 nm particles used here, and thus would be expected to travel through the nitrocellulose pores with even greater ease than the 400 nm particles, possibly resulting in differing flow patterns and particle velocities. Additionally, the charge of the polystyrene particles here may differ from the charge of nanoparticles made from different materials, such as gold or latex, and thus affect their electrostatic interactions with the membrane.

Experimentally, fluid was always observed to travel through the microscope field of view prior to the particle solution; this is assumed to be due to the surface tension and extremely small size of water molecules compared to particles. Wet-out flow, in which fluid travels through a material that is initially dry, is the situation observed and analyzed in macroscopic flow when the progression of the fluid front is measured.⁷² On the other hand, particles traveling within a fluid suspension are more accurately governed by principles of bulk flow.⁷³ An expected discrepancy in the velocity patterns between the macroscopic fluid front and microscopic fluid flow is that the macroscopic fluid front progresses more slowly as it travels further downstream, where particles within a fully-wetted membrane would theoretically travel at the same velocity regardless of their position along the length of the membrane.⁷⁴ Comparing these measured velocities would provide insight to how macroscopic flow, which is easier to measure, can be used to estimate microscale properties for precise design of more complex lateral flow assays and their constitutive biophysical reactions.

4. CONCLUSION

This document investigates some of the properties of lateral flow assays, mechanisms for the incorporation of multi-step processes, microfluidic characterizations, and their development for cervical cancer biomarker detection. Extensive further research is needed to collect the experimental and theoretical information that can definitively inform efficient prototyping of lateral flow assays for new applications as their need arises. The data presented here, however, provides a firm platform from which further experiments can be designed. Specifically, the method for quantifying particle flow through lateral flow assays offers many opportunities for further analysis with refined methods and an expanded scope of the properties investigated.

With regards to the lateral flow assay for cervical cancer detection, while future validation is needed, the results discussed here are a promising proof-of-concept and steppingstone for the incorporation of a new testing method for point-of-care cervical cancer detection. There are currently no cervical cancer protein biomarker detection methods that are commonly used, and such a method, if effective, could change the landscape of patient outcomes around the world. Triaging of patients in low-resource and rural areas would become more efficient, allocating limited resources to those that need it most and reducing the unnecessary cultural and emotional burden of clinical testing for those who do not need it. This is more than a biomedical engineering endeavor; it is an engineering, medical, public health and sociological undertaking that aims to holistically improve a necessary procedure in curbing preventable deaths from a lethal but treatable disease.

Ultimately, my hope is that the information presented here will provide future researchers with the framework to expand upon it in various directions. Thermally actuated wax valves can continue to be modified for incorporation in a variety of multi-step assays. μ PIV in porous membranes can inform robust microfluidic models and expedite the development of a wide range of paper-fluidic devices. Finally, a simple biomarker detection device for cervical cancer can be multiplexed to include additional or alternative biomarkers or otherwise modified as needed. The limitations of lateral flow assays today do not need to be cause for discarding them in favor of different methods, but rather can serve as one iteration in a continuous development process that can be improved upon by further experimentation and analysis.

APPENDIX A. CERVICAL CANCER

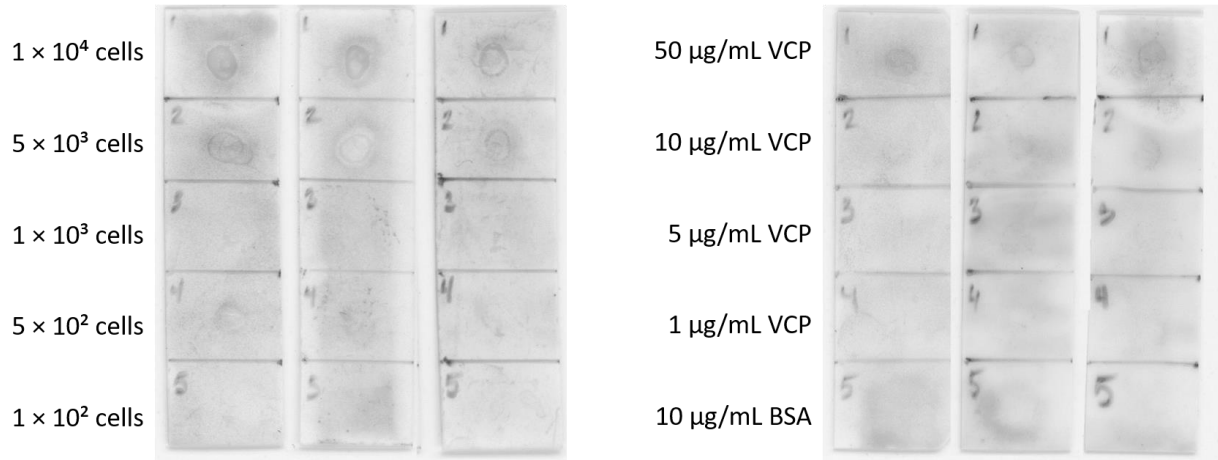


Figure 4.1: Dot blots comparing signal intensity from binding of M15 with HeLa cells and purified VCP to back-calculate protein concentration per cell count based on signal.

APPENDIX B. MACRO AND MICROFLUIDIC ANALYSES

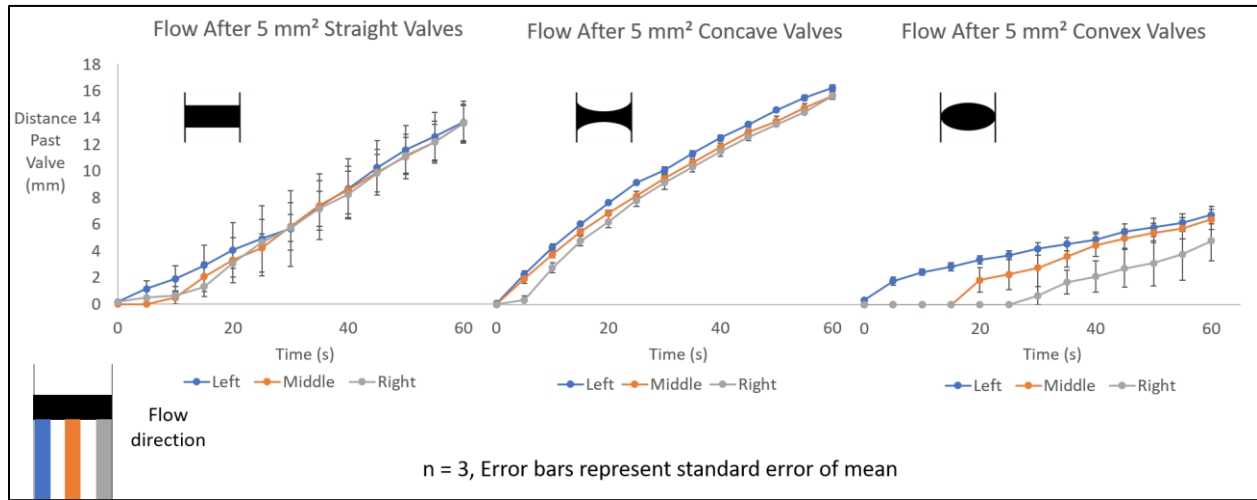


Figure 4.2: Flow rates for fluid through left edge, middle, and right edge of nitrocellulose membranes past 5 mm² straight, concave, and convex valves.

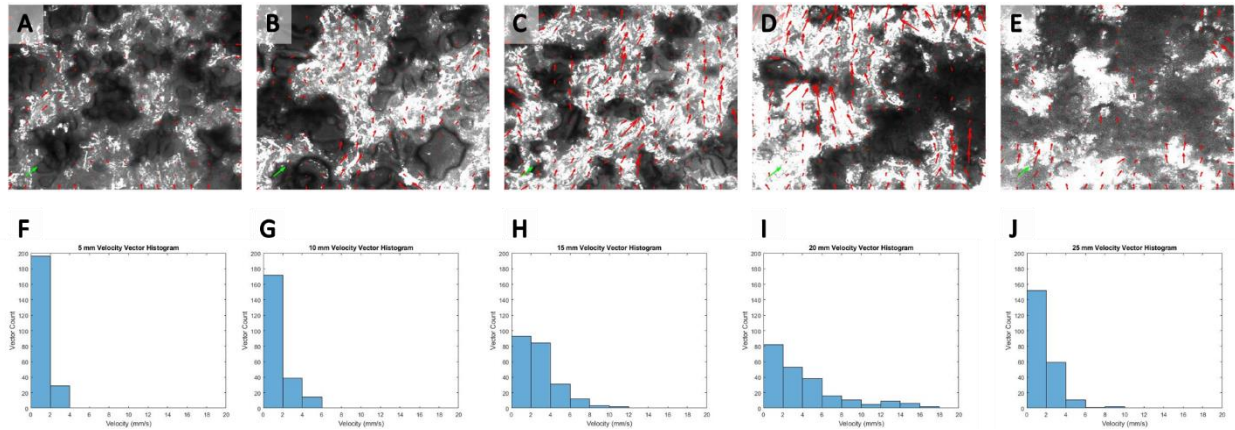


Figure 4.3: **Top:** All 400 images from a 10 second time series taken at the center of each membrane location combined into a single image to display locations of visible particles, with an overlaying vector field from EDPIV analysis (red arrows; green arrow represents the length of a 1 mm/s velocity vector in both the x and y directions). Locations are the following distances from the end of the strip: **A.** 5 mm **B.** 10 mm **C.** 15 mm **D.** 20 mm, and **E.** 25 mm. **Bottom:** Histogram reflecting the velocity distribution of all 225 vectors in each analysis. Locations are the following distances from the end of the strip: **F.** 5 mm **G.** 10 mm **H.** 15 mm **I.** 20 mm, and **J.** 25 mm.

REFERENCES

- 1 Mologic, Clearblue, <https://mologic.co.uk/case-studies/clearblue-the-first-one-step-pregnancy-test/>, (accessed May 5, 2020).
- 2 E. B. Bahadır and M. K. Sezgintürk, *TrAC Trends Anal. Chem.*, 2016, **82**, 286–306.
- 3 A. K. Yetisen, M. S. Akram and C. R. Lowe, *Lab. Chip*, 2013, **13**, 2210–2251.
- 4 M. Sajid, A.-N. Kawde and M. Daud, *J. Saudi Chem. Soc.*, 2015, **19**, 689–705.
- 5 K. M. Koczula and A. Gallotta, *Essays Biochem.*, 2016, **60**, 111–120.
- 6 E. Miller and H. D. Sikes, *Nanobiomedicine*, , DOI:10.5772/61114.
- 7 D. Gasperino, T. Baughman, H. V. Hsieh, D. Bell and B. H. Weigl, *Annu. Rev. Anal. Chem.*, 2018, **11**, 219–244.
- 8 K. Yamada, H. Shibata, K. Suzuki and D. Citterio, *Lab. Chip*, 2017, **17**, 1206–1249.
- 9 J. Hu, S. Wang, L. Wang, F. Li, B. Pingguan-Murphy, T. J. Lu and F. Xu, *Biosens. Bioelectron.*, 2014, **54**, 585–597.
- 10H. De Vuyst, L. Alemany, C. Lacey, C. J. Chibwasha, V. Sahasrabuddhe, C. Banura, L. Denny and G. P. Parham, *Vaccine*, 2013, **31**, F32–F46.
- 11M. Arbyn, E. Weiderpass, L. Bruni, S. de Sanjosé, M. Saraiya, J. Ferlay and F. Bray, *Lancet Glob. Health*, 2020, **8**, e191–e203.
- 12R. Landy, F. Pesola, A. Castañón and P. Sasieni, *Br. J. Cancer*, 2016, **115**, 1140–1146.
- 13A. G. Waxman, *Clin. Obstet. Gynecol.*, 2005, **48**, 77–97.
- 14S. J. Goldie, L. Gaffikin, J. D. Goldhaber-Fiebert, A. Gordillo-Tobar, C. Levin, C. Mahé and T. C. Wright, *N. Engl. J. Med.*, 2005, **353**, 2158–2168.
- 15K. Unger-Saldaña, A. Alvarez-Meneses and D. Isla-Ortiz, *J. Glob. Oncol.*, 2018, **4**, 221s–221s.
- 16Cervical cancer - Symptoms and causes, <https://www.mayoclinic.org/diseases-conditions/cervical-cancer/symptoms-causes/syc-20352501>, (accessed April 2, 2020).
- 17WHO | Cervical cancer, <http://www.who.int/cancer/prevention/diagnosis-screening/cervical-cancer/en/>, (accessed April 2, 2020).
- 18J. L. Belinson, R. G. Pretorius, W. H. Zhang, L. Y. Wu, Y. L. Qiao and P. Elson, *Obstet. Gynecol.*, 2001, **98**, 441–444.

- 19V. L. L, B. Ff, J.-S. R, B. M and S. T, *Obstet. Gynecol.*, 1993, **81**, 293–295.
- 20M. J. Huchko, J. Sneden, J. M. Zakaras, K. Smith-McCune, G. Sawaya, M. Maloba, E. A. Bukusi and C. R. Cohen, *PLoS ONE*, , DOI:10.1371/journal.pone.0118568.
- 21S. Consul, A. Agrawal, H. Sharma, A. Bansal, M. Gutch and N. Jain, *Indian J. Med. Paediatr. Oncol. Off. J. Indian Soc. Med. Paediatr. Oncol.*, 2012, **33**, 161–165.
- 22L. A. Denny, R. Sankaranarayanan, H. De Vuyst, J. J. Kim, P. O. Adefuye, L. Alemany, I. F. Adewole, O. A. Awolude, G. Parham, S. de Sanjosé and F. X. Bosch, *Vaccine*, 2013, **31**, F73–F74.
- 23X. Castellsagué, *Gynecol. Oncol.*, 2008, **110**, S4–S7.
- 24Fast Facts |, <http://www.ashasexualhealth.org/stdsstis/hpv/fast-facts/>, (accessed April 2, 2020).
- 25HPV and Pap Testing, <https://www.cancer.gov/types/cervical/pap-hpv-testing-fact-sheet>, (accessed April 2, 2020).
- 26T. C. Wright and L. Kuhn, *Best Pract. Res. Clin. Obstet. Gynaecol.*, 2012, **26**, 197–208.
- 27H. Kelly, P. Mayaud, M. Segondy, N. P. Pai and R. W. Peeling, *Sex. Transm. Infect.*, 2017, **93**, S36–S45.
- 28STD Facts - Human papillomavirus (HPV), <https://www.cdc.gov/std/hpv/stdfact-hpv.htm>, (accessed April 2, 2020).
- 29Cervical Cancer Causes, Diagnosis and Symptoms: NCCC, <https://www.nccc-online.org/hpvcervical-cancer/cervical-cancer-overview/>, (accessed April 2, 2020).
- 30E. I. O. Garner, *Cancer Epidemiol. Prev. Biomark.*, 2003, **12**, 242s–247s.
- 31W. William, A. Ware, A. H. Basaza-Ejiri and J. Obungoloch, *Comput. Methods Programs Biomed.*, 2018, **164**, 15–22.
- 32M. K. Quinn, T. C. Bubi, M. C. Pierce, M. K. Kayembe, D. Ramogola-Masire and R. Richards-Kortum, *PLoS ONE*, , DOI:10.1371/journal.pone.0044924.
- 33S. I. Mohammed, W. Ren, L. Flowers, B. Rajwa, C. J. Chibwasha, G. P. Parham and J. M. K. Irudayaraj, *Oncotarget*, 2016, **7**, 18787–18797.
- 34DOT Blot Protocol, <https://www.usbio.net/protocols/dot-blot>, (accessed March 24, 2020).
- 35L. Spence, 1.
- 36Dot Blot Protocol, <https://www.rndsystems.com/resources/protocols/dot-blot-protocol>, (accessed March 24, 2020).

- 37 Conjugation of Proteins to NHS-Activated Gold Nanoparticles, <https://www.cytodiagnosics.com/pages/conjugation-of-proteins-to-nhs-activated-gold-nanoparticles>, (accessed March 24, 2020).
- 38 VCP - Transitional endoplasmic reticulum ATPase - Homo sapiens (Human) - VCP gene & protein, <https://www.uniprot.org/uniprot/P55072>, (accessed March 24, 2020).
- 39 Western blot sample preparation | Abcam, <https://www.abcam.com/protocols/sample-preparation-for-western-blot>, (accessed March 25, 2020).
- 40 M. H. Jazayeri, H. Amani, A. A. Pourfatollah, H. Pazoki-Toroudi and B. Sedighimoghaddam, *Sens. Bio-Sens. Res.*, 2016, **9**, 17–22.
- 41 S. Puertas, M. Moros, R. Fernández-Pacheco, M. R. Ibarra, V. Grazú and J. M. de la Fuente, *J. Phys. Appl. Phys.*, 2010, **43**, 474012.
- 42 C. Parolo, A. de la Escosura-Muñiz, E. Polo, V. Grazú, J. M. de la Fuente and A. Merkoçi, *ACS Appl. Mater. Interfaces*, 2013, **5**, 10753–10759.
- 43 N. Tajima, M. Takai and K. Ishihara, *Anal. Chem.*, 2011, **83**, 1969–1976.
- 44 J.-M. Montenegro, V. Grazu, A. Sukhanova, S. Agarwal, J. M. de la Fuente, I. Nabiev, A. Greiner and W. J. Parak, *Adv. Drug Deliv. Rev.*, 2013, **65**, 677–688.
- 45 G. J. Worsley, N. Kumarswami, C. Minelli and J. E. Noble, *Anal. Methods*, 2015, **7**, 9596–9603.
- 46 K. M. Byers, A. R. Bird, H. D. Cho and J. C. Linnes, *ACS Omega*, 2020, **5**, 4673–4681.
- 47 N. M. Rodriguez, J. M. Brant, D. Pendharkar, H. Arreola-Ornelas, A. Bhadelia, G. de Lima Lopes and F. M. Knaul, *Am. Soc. Clin. Oncol. Educ. Book*, 2017, 416–425.
- 48 B. J. Toley, B. McKenzie, T. Liang, J. R. Buser, P. Yager and E. Fu, *Anal. Chem.*, 2013, **85**, 11545–11552.
- 49 S. Jahanshahi-Anbuhi, B. Kannan, K. Pennings, M. M. Ali, V. Leung, K. Giang, J. Wang, D. White, Y. Li, R. H. Pelton, J. D. Brennan and C. D. M. Filipe, *Lab. Chip*, 2017, **17**, 943–950.
- 50 L. Rivas, M. Medina-Sánchez, A. de la Escosura-Muñiz and A. Merkoçi, *Lab. Chip*, 2014, **14**, 4406–4414.
- 51 X. Sun, B. Li, C. Tian, F. Yu, N. Zhou, Y. Zhan and L. Chen, *Anal. Chim. Acta*, 2018, **1007**, 33–39.
- 52 B. R. Lutz, P. Trinh, C. Ball, E. Fu and P. Yager, *Lab. Chip*, 2011, **11**, 4274–4278.
- 53 E. A. Phillips, R. Shen, S. Zhao and J. C. Linnes, *Lab. Chip*, 2016, **16**, 4230–4236.
- 54 H. V. Hsieh, J. L. Dantzler and B. H. Weigl, *Diagnostics*, 2017, **7**, 29.

- 55 Y. Abdiche, D. Malashock, A. Pinkerton and J. Pons, *Anal. Biochem.*, 2008, **377**, 209–217.
- 56 D. G. Myszka, T. A. Morton, M. L. Doyle and I. M. Chaiken, *Biophys. Chem.*, 1997, **64**, 127–137.
- 57 C. L. A. Berli and P. A. Kler, *Microfluid. Nanofluidics*, 2016, **20**, 104.
- 58 T. Liang, R. Robinson, J. Houghtaling, G. Fridley, S. A. Ramsey and E. Fu, *Anal. Chem.*, 2016, **88**, 2311–2320.
- 59 J. G. Santiago, S. T. Wereley, C. D. Meinhart, D. J. Beebe and R. J. Adrian, *Exp. Fluids*, 1998, **25**, 316–319.
- 60 R. Lindken, M. Rossi, S. Große and J. Westerweel, *Lab. Chip*, 2009, **9**, 2551–2567.
- 61 Y. Mehmani and H. A. Tchelepi, *Adv. Water Resour.*, 2017, **108**, 83–98.
- 62 A. C. Marin, T. Grossi, E. Bianchi, G. Dubini and D. Lacroix, *Ann. Biomed. Eng.*, 2017, **45**, 1341–1351.
- 63 S. S. Datta, H. Chiang, T. S. Ramakrishnan and D. A. Weitz, *Phys. Rev. Lett.*, 2013, **111**, 064501.
- 64 A. Terzis, I. Zarikos, K. Weishaupt, G. Yang, X. Chu, R. Helmig and B. Weigand, *Phys. Fluids*, 2019, **31**, 042001.
- 65 W. Yun, C. M. Ross, S. Roman and A. R. Kavscek, *Lab. Chip*, 2017, **17**, 1462–1474.
- 66 J. C. Y. Guo, .
- 67 Y. Bazilevs and T. J. R. Hughes, *Comput. Fluids*, 2007, **36**, 12–26.
- 68 E. Pardoux and S. Zhang, *Probab. Theory Relat. Fields*, 1998, **110**, 535–558.
- 69 A. Koponen, M. Kataja and J. Timonen, *Phys. Rev. E*, 1997, **56**, 3319–3325.
- 70 E. A. Mason, A. P. Malinauskas and R. B. Evans, *J. Chem. Phys.*, 1967, **46**, 3199–3216.
- 71 Y. Villagrán Zaccardi, N. Alderete and N. De Belie, *MATEC Web Conf.*, 2018, **199**, 02019.
- 72 K. Li, D. Zhang, H. Bian, C. Meng and Y. Yang, *Sci. Rep.*, 2015, **5**, 1–7.
- 73 R. G. Cox and S. G. Mason, *Annu. Rev. Fluid Mech.*, 1971, **3**, 291–316.
- 74 Newton, Sir Isaac; Machin, John (1729). *Principia*. 1 (1729 translation ed.). p. 19.